JGR Earth Surface

RESEARCH ARTICLE
10.1029/2021JF006310

# Non-Monotonic Floodplain Responses to Changes in Flooding Intensity

**Eric A. Barefoot**[1,2], **Jeffrey A. Nittrouer**[1,3], **and Kyle M. Straub**[4]

[1]Department of Earth, Environmental and Planetary Sciences, Rice University, Houston, TX, USA, [2]Now at Saint Anthony Falls Laboratory, University of Minnesota, Minneapolis, MN, USA, [3]Now at Department of Geosciences, Texas Tech University, Lubbock, TX, USA, [4]Department of Earth and Environmental Sciences, Tulane University of Louisiana, New Orleans, LA, USA

**Key Points:**

- Flooding intensity controls the relative balance of lateral versus longitudinal sediment dispersal in experimental deltaic floodplains
- An optimum levee-building condition is attained at moderate levels of flooding

**Correspondence to:**
E. A. Barefoot,
eabarefoot@gmail.com

**Citation:**
Barefoot, E. A., Nittrouer, J. A., & Straub, K. M. (2021). Non-monotonic floodplain responses to changes in flooding intensity. *Journal of Geophysical Research: Earth Surface*, *126*, e2021JF006310. https://doi.org/10.1029/2021JF006310

Received 11 JUN 2021
Accepted 20 SEP 2021

**Abstract** Overbank flooding is common along most rivers, and it influences the dispersal of sediment to floodplains. While variable discharge is a critical aspect of fluvial landscape evolution, it is typically modeled by simplifying the hydrograph to an equivalent steady discharge: the channel-forming discharge. However, for all formulations used to simplify hydrographs, many different inputs can produce the same channel-forming discharge. Here, we investigate how hydrographs with different flood intensities affect channel mobility, sediment accumulation patterns, and alluvial morphology using a suite of physical experiments where a fan delta grew by dispersing a cohesive sediment mixture into a basin. The experiments spanned three levels: no flooding, low-intensity flooding, and high-intensity flooding, while the time-averaged water and sediment discharge was equivalent between all flooding regimes. Across this gradient, channel mobility, alluvial morphology and sediment dispersal scaled non-monotonically with flooding intensity, and the data suggest that levee-building feedbacks are the cause. We found that flood intensity modulates the relative balance between sediment delivery to channel margins, which nourishes levee growth, and the intensity of overbank flow, which inhibits levee growth. When flooding was absent, levees experienced consistent overbank flow and sediment delivery, leading to moderate levee aggradation and sporadic levee breaches. In contrast, when low-intensity flooding was imposed, levees experienced enhanced sediment delivery by low-amplitude floods, but only intermittent scouring. A further increase in flood intensity generated intense overbank flows that inhibited levee growth altogether. These results imply the existence of an optimum levee-building condition, where flooding conditions stabilize channels through levee-building feedbacks.

**Plain Language Summary** Flooding is a commonplace occurrence in natural rivers, and is necessary for depositing sediment on floodplains. However, most mathematical descriptions of how rivers change over time simplify variable discharge to an average value, omitting floods. Thus, it is not clear how floods affect river shape and sediment deposition on floodplains if the average discharge remains the same. To explore this question, we conducted three experiments, where a physical model of a river delta evolved while being subjected to one of three flood intensities: no flooding, low-intensity flooding, and high-intensity flooding, while the average discharge was the same for all three. We found that the intermediate state of low-intensity flooding was characterized by deep, slow-moving channels that had high levees. In contrast, both the high-intensity and the no-flooding experiments had wider, shallower, and faster-moving channels, but that high-intensity flooding produced the shallowest, widest, and fastest channels. We identified that the river levees were the cause of this behavior. High-intensity floods prevented levees from growing by spreading sediment widely across the floodplain, whereas a complete lack of flooding starved the river banks of sediment. These results imply that the optimum levee-building condition lies between these two extreme states.

## 1. Introduction

Rivers experience variable discharge conditions over time, and the hydrograph defines the frequency and magnitude distribution of flow and sediment transport events. The integrated history of flow determines channel dimensions and mobility, which directs sediment dispersal and shapes the morphology of rivers and deltas (Pickup & Rieger, 1979). However, due to the complexity associated with morphodynamic feedbacks, it is common when modeling fluvial channel and landscape development to simplify the hydrograph

into a characteristic steady discharge; namely, the channel forming discharge (Leopold & Maddock Jr., 1953; Wolman & Miller, 1960).

An issue with this approach is that the methods used to calculate a characteristic discharge do not produce unique solutions: many different types of hydrographs can be summarized to generate the same characteristic value. One formulation used by Blom et al. (2017) exemplifies the strategy. Blom et al. (2017) consider a hydrograph composed of only two flows that transport sediment according to an appropriate sediment transport relation (e.g., Engelund & Hansen, 1967), a maximum flow ($Q_{max}$) and a minimum flow ($Q_{min}$), and express the equivalent steady sediment discharge ($\bar{Q}$) as:

$$\bar{Q} = \alpha Q_{min} + (1 - \alpha) Q_{max}, \tag{1}$$

where $\alpha$ is the occurrence frequency of $Q_{min}$, and the frequency of $Q_{max}$ is by definition $(1 - \alpha)$. In Equation 1, $\alpha$ can be termed a flood *intermittency* (Parker et al., 1998), and the difference between $Q_{max}$ and $Q_{min}$ is the flood *magnitude* (Latrubesse et al., 2005).

Importantly, this and other approaches are intended to be used to calculate equilibrium sediment transport conditions and other system properties like channel geometry (Blom et al., 2017; Naito & Parker, 2019). Tuned to capture specific processes and aspects of the morphodynamic system, models using this approach yield insight about these processes, but are difficult to generalize.

Consequently, predictions for channel geometry and sediment transport can contradict each other depending on the formulation used to calculate the equivalent constant flow. For instance, Blom et al. (2017) indicate that all else being equal, an increase in flow variability generates an increase in channel width; this supposition is supported by experimental studies and field research (Eschner et al., 1981; Esposito et al., 2018). However, recent numerical modeling studies by Naito and Parker (2019) found that channel width decreases as flow variability increases, because enhanced floodplain aggradation builds banks that confine flow and constrict the channel. This supposition is supported by field observations from sand-bed channels (Pizzuto, 1986).

Importantly, while these mathematical models and many others highlight lateral channel migration as the main process driving mobility, they can broadly be considered to represent channel morphology at steady state between avulsions, when the channel abruptly relocates to a new position on the floodplain. In this particular case, the discrepancies between models appear to arise because each formulation describes sediment exchange between the channel and floodplain differently. Generally speaking, it is known that in order to faithfully model many floodplain processes, a variable hydrograph is required (Lauer & Parker, 2008), yet the appropriate formulation is not clear, as the impact of overbank floods on sediment transport processes at the basin scale remains underconstrained. To cast light on this issue, the present study defines a parameter, *flood intensity* ($Q_v$), as the ratio of $Q_{max}$ and $Q_{min}$,

$$Q_v = \frac{Q_{max}}{Q_{min}}, \tag{2}$$

provided that $\alpha$ changes to maintain a constant $\bar{Q}$. By substituting Equation 2 into Equation 1, an expression for $\alpha$ may be derived in terms of $Q_v$, $Q_{min}$, and the chosen equivalent constant discharge: $\bar{Q}_c$,

$$\alpha = \frac{\frac{\bar{Q}_c}{Q_{min}} - Q_v}{1 - Q_v}. \tag{3}$$

In field-scale systems, $\bar{Q}_c$ would likely be analogous to the channel-forming discharge, but in the present study, it is taken as the mean discharge. In this way, $Q_v$ describes the flow fluctuations relative to a baseline, and allows changes in the hydrograph to be separated from adjustments in the equivalent steady flow. This is of critical importance because while variable discharge is recognized to impact channel mobility and sediment transport, it remains challenging to parse the relative effects of flood magnitude, intermittency, and fluvial response to an equivalent steady flow.

For example, channel mobility scales with both water discharge and sediment supply (Bryant et al., 1995), but Esposito et al. (2018) show similar results with only a change in $Q_v$. Bolstering this assertion, numerical modeling presented by Naito and Parker (2019) demonstrates the importance of flood intensity on bank erosion. Experiments also show that flow variability is coupled to overbank erosion and chute cut-offs

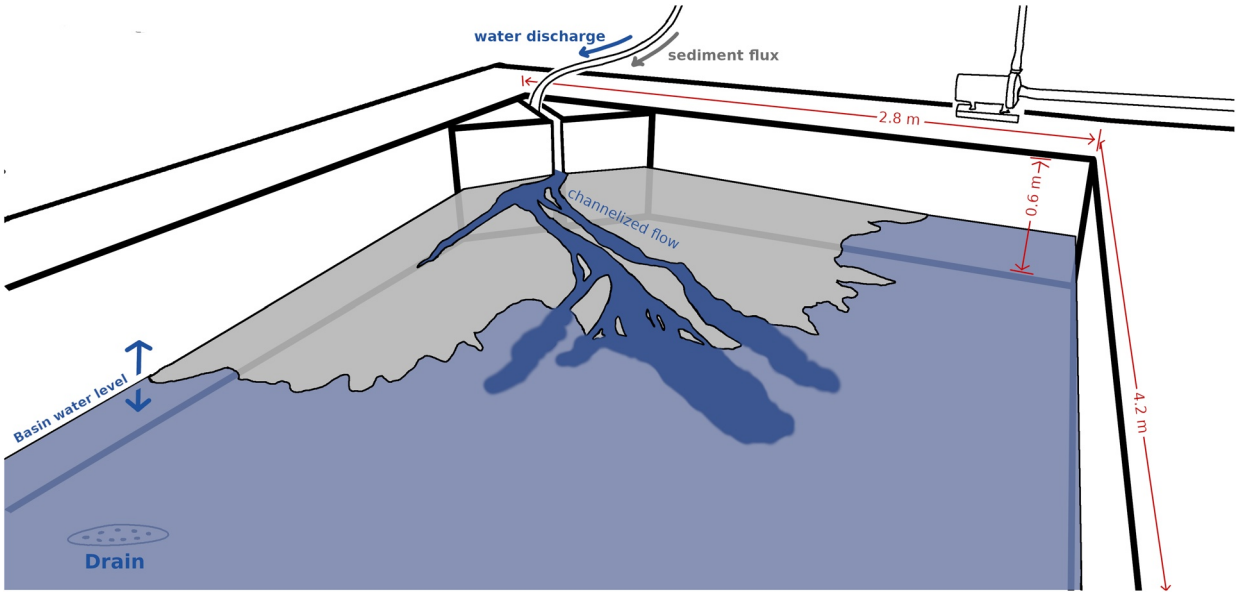


**Figure 1.** The Tulane University Delta Basin measures 4.2 m × 2.8 m × 0.6 m. Water and sediment are fed from a funnel and pipe system, where the pump for water and feed rate of sediment are controlled on a 30-s basis from a central computer. Water and sediment exit the inlet channel and form a delta in the corner of the basin, that can therefore spread over a 90° swath of the basin. Channels form on the delta topset and direct water and sediment to the shoreline. Water level is controlled via a computer-operated weir (not shown) that is hydraulically connected to the drain on the floor of the basin. By moving the weir vertically, the water level can be controlled with sub-millimeter precision.

(Van De Lageweg et al., 2013), in addition to levee building and in-channel sediment aggradation (Esposito et al., 2018), all of which play critical roles in the channel avulsion process (Mohrig et al., 2000). Modern systems characterized by highly seasonal discharge exemplify this feedback, where both lateral migration and avulsion frequency are enhanced relative to rivers with muted hydrographs (Fielding et al., 2018; Leier et al., 2005). Meanwhile, an increase in flood intermittency can suppress channel mobility because of sediment reworking during low-flow conditions that entrench channels (Miller et al., 2019)

This study quantifies floodplain morphodynamic feedbacks across a gradient of flooding intensity ($Q_v$). By using $Q_v$ as the independent variable, we separate changes in flow variability from changes in equivalent steady discharge, and characterize the main ways in which variable flow influences channel mobility, sediment dispersal, and alluvial morphology in an experimental fan delta.

## 2. Methods

### 2.1. Experimental Design

A suite of physical experiments were conducted in the Tulane University Delta Basin where fan deltas evolved in response to three discrete flooding regimes: no flooding ($Q_v$ = 1), low-intensity flooding ($Q_v$ = 1.5), and high-intensity flooding ($Q_v$ = 3). The basin has dimensions of 4.2 m × 2.8 m × 0.6 m, and sediment and water were mixed and fed into the basin from an inlet channel, forming a fan delta that spread radially up to 90°(See Figure 1). The feed rate of sediment and water at the apex is set by a computer-controlled commercial feeder and pump, respectively, and water drains from the delta basin via a computer-controlled weir that maintains basin water level with sub-millimeter precision. The experiments featured long-term aggradation, which was induced by steadily raising the water level throughout the experiment. The water-level-rise rate is calibrated to generate accommodation equal to the long-term sediment-feed rate, so that the average radial shoreline was dynamically stable through time (Straub et al., 2015). The sediment used in this experiment was a mixture of coarse sand, fine sand, and silica flour, with additives that impart cohesion. The initial grain-size distribution of the mixture is thus bimodal, with one peak at 1,000 $\mu$m, and a second at 100 $\mu$m. This mixture enhances channelization compared to cohesionless mixtures, generating rich channel-floodplain interactions and delta lobe-switching via avulsions (Hoyal & Sheets, 2009).

**Table 1**
*Control Parameters for Tulane University Delta Basin for Experiment Spanning Three Levels of a Gradient of $Q_v$*

| | No flooding | Low-intensity | High-intensity |
|---|---|---|---|
| Flood Intensity ($Q_v$, —) | 1.0 | 1.5 | 3.0 |
| Flood discharge (L/s) | 0.172 | 0.213 | 0.426 |
| Baseline discharge (L/s) | 0.172 | 0.142 | 0.142 |
| Equivalent constant discharge (L/s) | 0.172 | 0.172 | 0.172 |
| Sediment concentration ($Q_s/Q_w$) | 0.001 | 0.001 | 0.001 |
| Basin water level rise rate (mm/hr) | 0.25 | 0.25 | 0.25 |
| Flood cycle time ($T_f$, min) | 30 | 30 | 30 |
| [a]Compensation time scale ($T_c$, hrs) | 50 | 50 | 50 |
| Total run time (hrs) | 100 | 100 | 100 |

[a]This value estimated from Li et al. (2016).

Over the duration of the experiment, the sediment mixture, rate of basin water-level rise, and the time-averaged sediment and water flux, were all held constant (Table 1). In field scale systems, the water-to-sediment ratio transported in rivers is not constant with variable flow (Nittrouer et al., 2008). However, we chose to hold the water-to-sediment ratio constant, similarly to other experiments (Esposito et al., 2018), since the sediment concentration-discharge scaling differs between field systems, and it is not well understood what controls this scaling. In this way, choosing a constant ratio simplifies the analysis, and provides a baseline for future studies with other concentration-discharge relations, which are beyond the scope of this study. Floods were designed as a Gaussian function of time (Equation 4). This permitted the intermittency and magnitude of floods to smoothly covary while maintaining a constant integrated discharge over every flood cycle despite changes in amplitude. In this way, the effect of hydrograph fluctuations was separated from changes in overall water and sediment flux. Discharge over every flood cycle was thus defined in reference to an equivalent constant discharge ($\bar{Q}_c$), and $Q_{min}$ was defined as a fraction of $\bar{Q}_c$, such that $Q_{min} = k\bar{Q}_c$. In this way, over a flood cycle of duration $T_f$, discharge is given as:

$$Q(t) = k\bar{Q}_c\left(1 + (Q_v - 1)e^{-\left(\frac{k\sqrt{\pi}(Q_v-1)}{(k-1)T_f}t\right)^2}\right) \quad (4)$$

on the closed domain $[-T_f/2, +T_f/2]$. For this experiment, $k = 0.825$ and $T_f = 30$ minutes, where sediment and water were specified every 30 s, yielding an experimental hydrograph (see Figure 2).

A flood interval of 30 min is chosen because it is frequent relative to autogenic cycles of sediment storage and release (Kim et al., 2006), ensuring that sedimentary dynamics were not impacted by individual flood events, but rather influenced by flooding as a background condition (Miller et al., 2019). Since the primary depositional process occurring in this experimental apparatus is the successive emplacement of delta lobes, the appropriate autogenic timescale for this comparison is the *compensation timescale* ($T_c$), defined as the ratio of the characteristic topographic relief ($l$) to the long-term aggradation rate ($r$; Wang et al., 2011), that is:

$$T_c = \frac{l}{r}. \quad (5)$$

Over a duration of time $T_c$, depositional lobes stack such that sediment is spread evenly over the delta topset. In this experimental apparatus, $T_c \approx 50$ hours (Li et al., 2016), and given the flood cycle duration, ~ 100 floods occurred for each $T_c$. Each experimental data set comprises a 100 h episode of experimental run time,

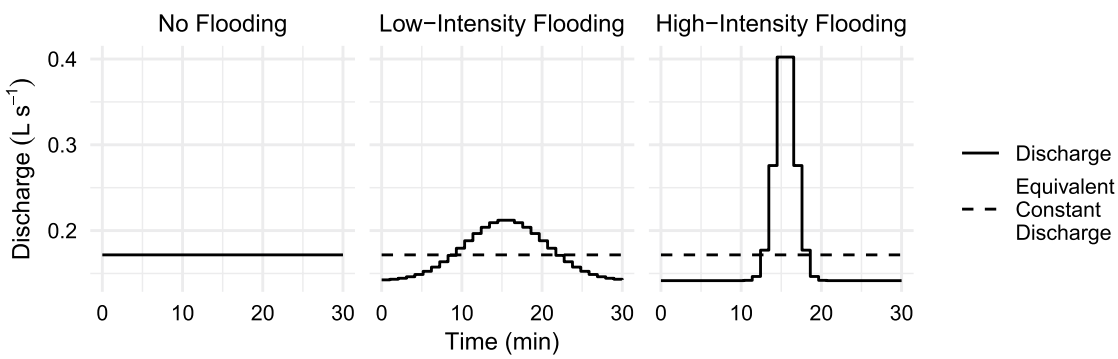


**Figure 2.** Flood pulse design for experimental runs computed using Equation 4. From left to right, these flood pulses exemplify flooding intensity for $Q_v = 1.0$, $Q_v = 1.5$, and $Q_v = 3.0$. The baseflow discharge ($Q_{min}$) is 82.5% of the equivalent constant discharge ($\bar{Q}_c$).

equivalent to ~$2 \times T_c$. This ensures that sufficient time elapsed to characterize the dynamic equilibrium of the delta, and that measured quantities were statistically stationary.

It is not clear, *a priori*, how floods in sedimentary experiments should be scaled to best compare with field systems. Esposito et al. (2018) demonstrated that floods act to change river dynamics by changing mobility and sediment exchange between the channel and the floodplain. The largest floods in this experiment match those used by Esposito et al. (2018), which were planned to approximate $Q_v$ in large river systems like the Mississippi. However, when $Q_v = 3$, the dynamics and morphology of those experimental deltas more strongly resembled the dynamics of braided rivers than sinuous lowland rivers. In fact, unpublished trials conducted prior to Esposito et al. (2018) indicate that flooding more intense than $Q_v = 3$ in this apparatus substantially retards channel development. Thus, $Q_v = 3$ may be the maximum flood intensity allowed in this apparatus, but in natural river channels, $Q_v$ can often be much larger than three (Plink-Björklund, 2015). The intermediate flood intensity value was chosen to be $Q_v = 1.5$ because at this value, the "flood wave" spanned the entire flood cycle of 30 min, and therefore is the lowest intensity flood we can impose while maintaining the same recurrence interval. In essence, we chose the flood intensity values to encompass the maximum value that still produces channels, as well as the minimum feasible value for the apparatus.

In field scale systems, there exist myriad processes that influence sediment exchange and channel mobility, including vegetation (Parker et al., 2011) and floodplain hydrology (Mertes, 1994), among others. Finding a direct process-similarity between these experiments and the field is likely not advisable. Rather, a particular value of $Q_v$ should be considered in the context of the processes that dominate sediment exchange between channels and overbank environments. Using this framework, these experiments are designed to represent the response of the delta system across the maximum range of $Q_v$ values that preserve channel formation for a given system, and capturing intermediate levels.

### 2.2. Data Collected

Two main types of data—topography and imagery—were collected from these experiments to constrain channel mobility, sediment dispersal, and fluvial morphology.

For every hour of runtime, topographic data were collected using a terrestrial lidar scanner. The 3D point-cloud data were then gridded and averaged at a horizontal resolution of $5 \times 5$ mm to produce a vertical resolution of <1 mm. Rarely, a topographic scan failed (~0.2% of all scans), and since some analysis of scan data can be biased by gaps in the record, the missing data was interpolated on a pixel-by-pixel basis using the closest complete scans before and after. Topographic scans were then clipped to the basin water level, and used to generate masks of the delta topset and identify the shoreline. Sequential scans were then post-processed to generate synthetic stratigraphy, where each topographic surface was clipped to reflect subsequent erosion such that only preserved depositional surfaces remained (Strong & Paola, 2008).

Throughout the experiment, overhead images were collected every 15 min to capture each flood peak and trough, then corrected for lens distortion using Agisoft Metashape. Images also occasionally failed to capture (~0.1% of all images), and the missing data were discarded. For analysis, images were projected into the reference frame for topographic scans, and resampled to 5 mm × 5 mm pixel resolution. The area comprising basin water was then clipped in every image using the topographically derived topset mask, with the remainder analyzed to identify channel locations. Blue dye was injected into the water for every overhead image, so channels were manually mapped to create one channel mask for every hour of runtime to generate a data set of 300 masks (100 for each experiment; Figure 3). Since the dye was only added for a brief period (30 s) in order to capture overhead photographs, subsequent clear water flow cleansed the delta surface of excess blue dye, ensuring that the intensity of blue color faithfully discriminates between "wet" from "dry" pixels. We additionally mapped the channels based on observing morphological features of the delta, excluding patches of blue that were associated with the shoreline or overbank flow.

Additionally, in every run hour, levee breaches were located and counted from overhead imagery. Levee breaches were identified in overhead images as locations on the channel banks where water escaped the channel during low flow. In this way, the count estimate reflects locations of potential failure during subsequent floods, rather than locations of overbank flow during floods.

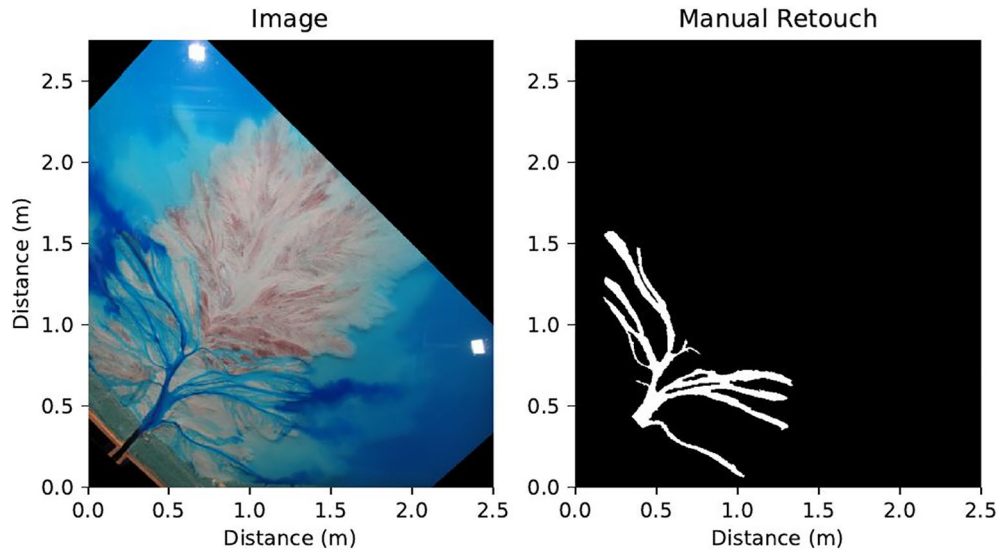


**Figure 3.** Channels were manually mapped to generate channel masks for each run hour of the experiment.

At the end of the experimental run, the deposit was drained and dried, then cut along four strike sections. Each of these cuts was imaged and georeferenced to the basin, generating orthophotos of the face. Facies were interpreted in the cuts based on deposit geometries revealed by corresponding synthetic stratigraphy sections. Samples were taken from several locations in each cut, chosen to capture major facies. Grain-size distributions for these samples were generated using a laser particle size analyzer.

### 2.3. Channel Mobility

As channels migrate laterally and avulse, the area occupied by channels decorrelates from its initial state as a function of time because channels visit new locations on the floodplain. Using channel mask data, correlation is described in terms of pixels, where the more pixels that change from "wet" to "dry," the less two channel images overlap (Wickert et al., 2013). Thus, the normalized channel overlap between any pair of images, $O_\Phi$ is given as:

$$O_\Phi = 1 - \frac{D}{A\Phi}, \tag{6}$$

where $D$ is the number of pixels that changed, $A$ is the total number of pixels in the image, and $\Phi$ is a dimensionless parameter that gives the number of pixels that would be expected to change by randomly scattering wet and dry pixels across the surface (Wickert et al., 2013). Between two images, 1 and 2, $\Phi$ is expressed as:

$$\Phi = (w_1 d_2 + w_2 d_1), \tag{7}$$

where $w_x$ and $d_x$ are the fraction of wet and dry pixels in images 1 or 2. Theory dictates that channels will decorrelate according to an exponential decay function of the lag time between successive channel maps (Wickert et al., 2013):

$$O_\Phi = (a_M - p_M)e^{-Mt} + p_M, \tag{8}$$

where $O_\Phi$ is given in Equation 6, $t$ is the lag time between masks, and $p_M$, $a_M$ and $M$ are constants. To quantify channel mobility using this method, the normalized overlap between successive channel masks was measured for each experiment, and an exponential model was fit for each data set using Equation 8 by restricted maximum likelihood (Venables & Ripley, 2002). The mobility of channels is interpreted using the reciprocal of the exponential decay constant ($1/M$), i.e., an $e$-folding time. Higher $e$-folding times imply immobile channels that decorrelate slowly, because channels remain in the same location over long lag times, whereas small $e$-folding times imply mobile channels.

### 2.4. Sediment Dispersal

To evaluate the spatial heterogeneity of sediment dispersal and patterns of deposition in the fluvio-deltaic system, four approaches are employed. In the first, the spatial variation of sediment deposition was qualitatively assessed using isopach maps and circular sections constructed from synthetic stratigraphy. Spatial patterns of deposition are revealed by comparing isopach maps for equivalent intervals of each experiment, and circular sections highlight lateral variation in sediment thickness.

The second method quantifies the evenness of lateral sediment dispersal by measuring the completeness of stratigraphic columns as a function of discretization time, that is, the precision of timing that is desired for interpretation. Since episodes of deposition are interspersed with hiatuses in the stratigraphic record, the history of accumulation in any given location is incomplete. Stratigraphic completeness is commonly defined as:

$$f_c \equiv \frac{n\delta t}{\hat{t}}, \tag{9}$$

where $\delta t$ is the discretization time, that is, how finely the stratigraphic record is divided. $n$ is the number of time intervals represented by sediment, and $\hat{t}$ is the total time encompassed by the stratigraphic column (Straub et al., 2020). Importantly, if the stratigraphic record is finely divided into small units of time ($\delta t$), the number of time intervals represented by sediment ($n$), goes down. This is an expression of the Sadler effect, and the completeness ($f_c$) grows as a power-law function of the discretization time:

$$f_c = \left(\frac{\delta t}{\hat{t}}\right)^{\beta} \tag{10}$$

The exponent $\beta$, which is $-1\times$ the Sadler exponent, takes on values between zero and one, and has physical meaning; it scales with the spatial uniformity of sediment deposition (Sadler, 1981; Jerolmack & Sadler, 2018).

Completeness naturally has a restricted range from 0 to 1. The stratigraphic record can be at minimum 0% complete, and above a critical averaging timescale, the stratigraphic record will essentially always represent some deposition, so the relationship will saturate at $f_c = 1$. However, in between these bounds, the data are well-described by a power-law. For these experiments, the critical timescale is the compensation timescale ($T_c$), because it is at that discretization time that one expects to see delta lobes evenly spread across the topset. In this way, using stratigraphic columns extracted from circular sections of the experimental data, $f_c$ was calculated for each column across a range of $\delta t$ values. These data were then fit with Equation 10 using Markov Chain Monte-Carlo (MCMC) sampling methods, and the posterior distributions of $\beta$ were interpreted.

The third method for characterizing spatial patterns of sediment deposition measures the abundance of channel deposits in the strata. High channel mobility and even sedimentation will increase the amount of channel deposits, whereas low channel mobility will spatially restrict channel deposits, resulting in overall lower representation in the stratigraphy (Leeder, 1977; Chamberlin & Hajek, 2015). Synthetic stratigraphy was used to sub-sample channel-mask data and produce a data set showing the abundance of channel deposits throughout the stratigraphic volume. The relative abundance of channels in each experiment was then quantified as the fraction of the deposit in different stratigraphic cuts that was channel or floodplain.

Finally, we qualitatively assessed spatial grain-size fractionation in the stratigraphy using images of the physical stratigraphic strike sections. In the experiment, red sand was added as a tracer for the coarse sediment fraction, so an abundance of red sediment in the deposit is indicative of coarse deposition, whereas white sediment is indicative of fine deposition. Coarse and fine fractions were mapped for each experimental interval in both a proximal and distal section.

### 2.5. Delta-Floodplain Morphology

To document changes in channel morphology throughout each experiment, average estimates of channel width, depth, and slope were produced for each experiment. To measure channel geometries, circular sections were taken across each channel mask at designated radii, and channel banks were identified as points where the edges of channels intersected the section. Channel width was then measured as the distance

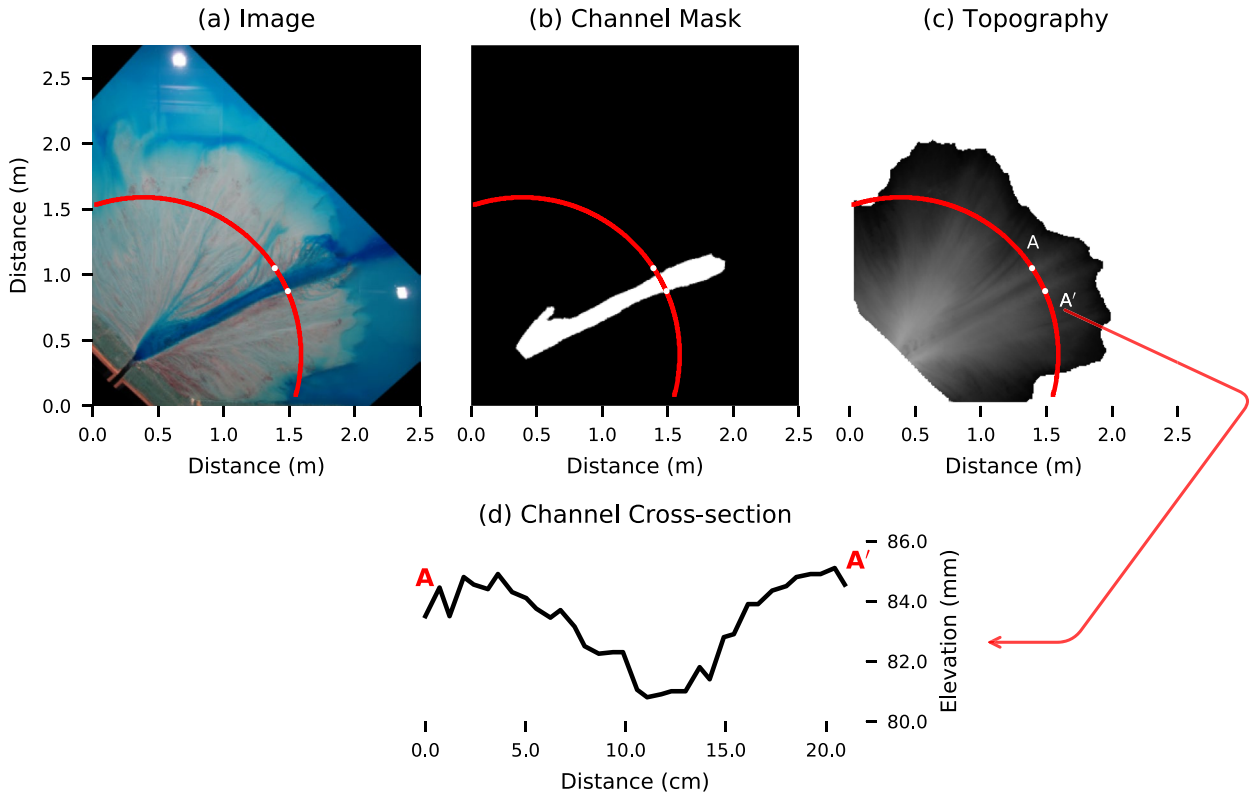


**Figure 4.** In order to extract channel dimensions from coupled topography and overhead imagery data, images were georeferenced to the topography. Circular sections were taken, and changes from "dry" to "wet" (0–1) were identified, which defined the left and right bank of the channel. The channel width was taken as the distance between the points, and a line of pixels between the corresponding points were extracted from the topography, and the total relief was taken as the channel depth. Channel slope was measured by extracting all topographic points where the channel mask was "wet" and a least squares fit was applied to the elevation as a function of radius from the apex.

across the channel between points on the banklines, and topographic data was extracted along this transect. Channel depth was measured as the total topographic relief along this channel transect (see Figure 4). The vertical resolution of the topographic measurements is often an appreciable fraction of the channel depth (~25% in Figure 4). While this adds uncertainty to the estimates, this uncertainty generally remains less than the variation in the data. Channel slope was estimated by extracting topography within each channel mask, and fitting a linear regression to the topography data along radial transects from apex to shoreline. The trends for these parameters are averaged over the whole duration of the experiment. Thus, these estimates approximate a steady-state equilibrium geometry, averaged over many avulsion and flood cycles. Additionally, throughout the experiment, there were occasionally multiple active channels. However, it was not possible to determine flux partitioning between distributary channels, so rather than attempt to calculate discharge-normalized channel dimensions for comparison, we simply measured the dimensions of all channels, and accepted this factor as a source of noise in our data.

Changes in floodplain and deltaic morphologies, including the average delta topset slope and topographic relief were also documented. Delta topset slopes were calculated by extracting average radial topographic profiles from the delta apex to the shoreline. Floodplain relief was estimated by detrending the delta topset using the calculated slopes and computing the vertical distance from the $25^{th}$ percentile to the $95^{th}$ percentile of the detrended elevation data (see Figure 5).

The shoreline was defined as the line where the topographic data intersected the water surface elevation in the basin. Shoreline rugosity ($R$) was computed as the coefficient of variation in radial distance between every point on the shoreline and the delta apex:

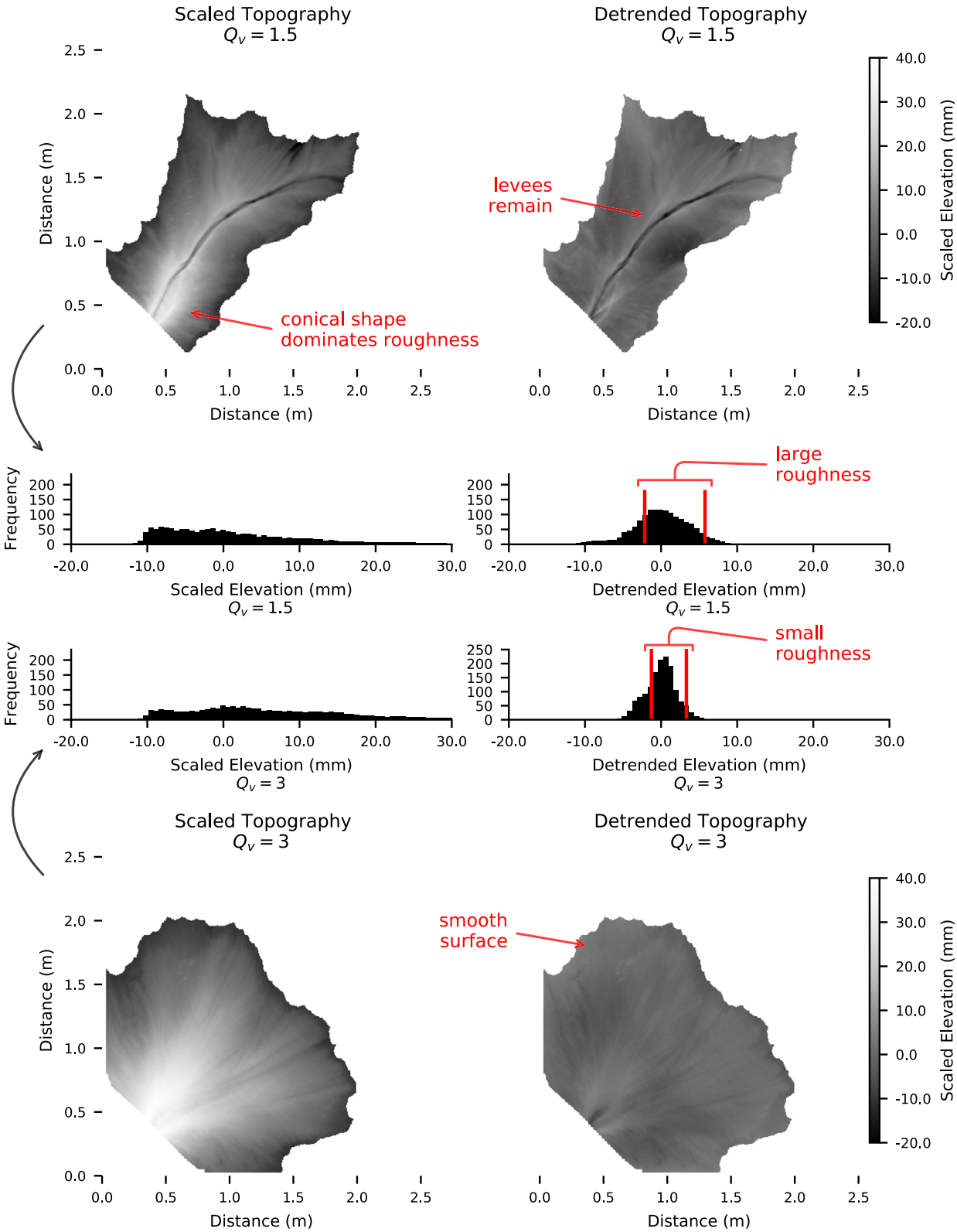
Scaled Topography
$Q_v = 1.5$
Detrended Topography
$Q_v = 1.5$
Distance (m)
Scaled Elevation (mm)
conical shape
dominates roughness
levees
remain
Frequency
Scaled Elevation (mm)
$Q_v = 1.5$
Detrended Elevation (mm)
$Q_v = 1.5$
large
roughness
$Q_v = 3$
$Q_v = 3$
small
roughness
Scaled Topography
$Q_v = 3$
Detrended Topography
$Q_v = 3$
smooth
surface

**Figure 5.**

**Table 2**
*Posterior Estimates or Maximum-Likelihood Estimates for Observed Delta Parameters*

| | $Q_v = 1$ | $Q_v = 1.5$ | $Q_v = 3$ |
|---|---|---|---|
| Channel depth (mm) | 10.5 ± 0.285 | 12.5 ± 0.402 | 8.98 ± 0.33 |
| Channel width (mm) | 6.83 ± 0.194 | 5.76 ± 0.249 | 16.5 ± 0.496 |
| Channel slope ($m/m \times 10^{-2}$) | 2.67 ± 0.015 | 1.83 ± 0.013 | 2.69 ± 0.012 |
| Shoreline rugosity (—) | 0.18 ± 0.005 | 0.356 ± 0.004 | 0.137 ± 0.005 |
| Delta topset roughness (mm) | 4.91 ± 5.25 | 7.53 ± 2 | 4.74 ± 4.38 |
| Delta topset slope ($m/m \times 10^{-2}$) | 2.93 ± 0.02 | 4.37 ± 0.06 | 3.58 ± 0.03 |
| Sediment dispersal ($\beta$) | 0.462 ± 0.024 | 0.507 ± 0.028 | 0.391 ± 0.039 |
| Channel mobility (hrs)[a] | 19.8 ± 1.44 | 23.9 ± 2.24 | 4.59 ± 0.244 |
| Levee breaches | 9.03 ± 0.296 | 5.11 ± 0.224 | 10.6 ± 0.342 |

*Note*. Posterior estimates are given as the mean ± standard deviation.
[a]Estimates made with maximum-likelihood are given as mean ±95% confidence intervals.

$$R_j = \sqrt{\frac{1}{N}\sum_{i=1}^{N}\left(\frac{r_{i,j} - \overline{r}_j}{\overline{r}_j}\right)^2}, \tag{11}$$

where $R_j$ is the rugosity of the shoreline at time $j$, $r_{i,j}$ is the distance from the apex to all points that define the shoreline in image $j$. $\overline{r}_j$ is the mean distance from the delta apex to the shoreline in image $j$, and $N$ is the total number of spatial points that define the shoreline.

## 3. Results

### 3.1. Channel Mobility

Estimates of the $e$-folding time for channel overlap decay (Equation 8) indicate that channel mobility scaled non-monotonically with flooding intensity. In the no-flooding experiment, the channel overlap $e$-folding time was 19.8 h. When low-intensity flooding was imposed, the $e$-folding time increased to 23.9 h, an increase of ~20.7%. However, when flood intensity increased to $Q_v = 3$, the $e$-folding time decreased to 4.59 h, a decrease of ~76.8% from no-flooding. In terms of $T_c$, the $e$-folding time for no flooding is 39.6% $T_c$, compared to 47.8% $T_c$ for low-intensity flooding and 9.18% $T_c$ for high-intensity flooding (see Table 2 and Figure 6).

### 3.2. Sediment Dispersal

Channel and floodplain morphodynamics impact sediment dispersal in the fluvial system, which manifests as the spatial unevenness of sediment deposits. Isopach maps prepared for each flooding regime demonstrate that sedimentation is evenly distributed across the delta topset in the high-intensity flooding experiment, highly localized when $Q_v = 1.5$, and intermediate when no flooding is present (Figure 7). In particular, isopach maps show that when low-intensity flooding is imposed, deposition is localized along alluvial ridges, generating clearly visible levee deposits (Figure 7, panel b). Meanwhile, deposition is also focused at the channel mouth, where the delta builds elongate lobes. Synthetic stratigraphic sections corroborate this observation, where thin lateral deposition adjacent to the floodplain is contrasted with thick levee deposits in proximal sections, but additional lobe deposition can be seen in the most distal cut.

**Figure 5.** To remove the overall conical trend and estimate the surface roughness of the topset, each topographic surface was vertically displaced to be centered on zero (Scaled Topography), and radial transects were taken from the apex to shoreline, and all pixels along the transect were detrended by the slope of the transect (Detrended Topography). Histograms of the elevation images are shown before and after, demonstrating that this procedure removes the long-wavelength topography and retains roughness features like levees. The roughness was taken as the distance from the $25^{th}$ to $95^{th}$ percentiles of the detrended histogram, chosen because the distributions of elevation are generally right-skewed.

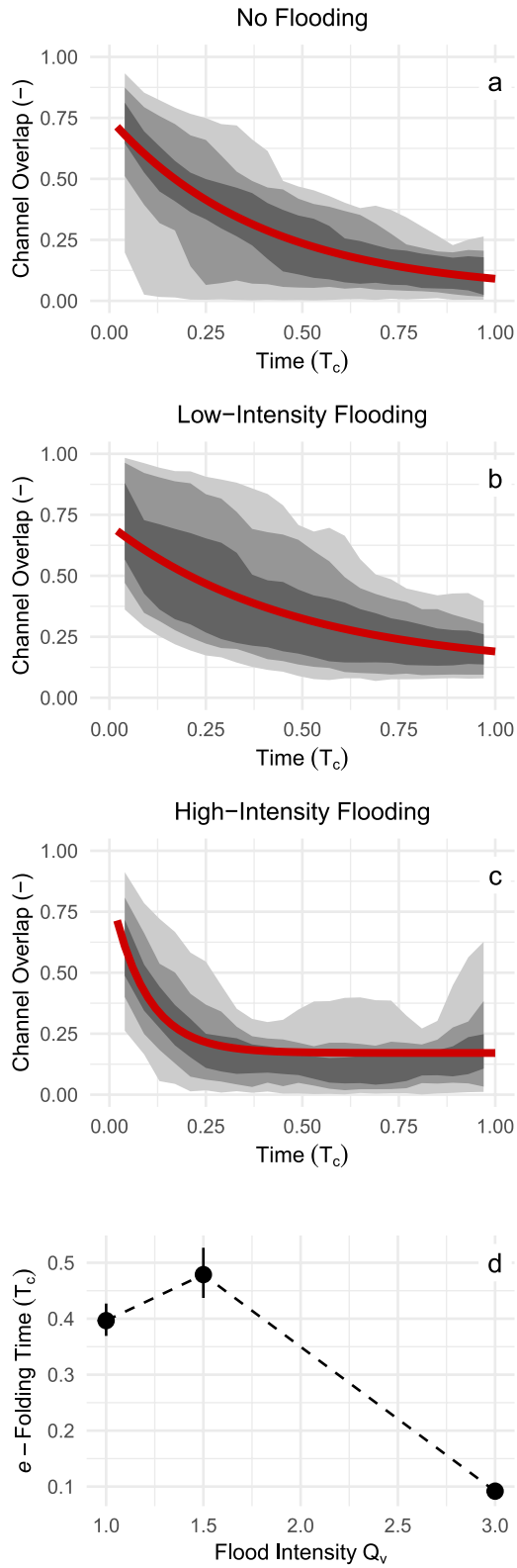


**Figure 6.** Panels (a–c) shows the decay of normalized channel overlap with successive lag times. The shaded regions show the distribution of the data, with the lightest band showing the 1–99th percentiles, the middle band showing the 10–90th percentiles, and the darkest showing the 25–75th percentiles. The red lines show model fits using Equation 8. Panel (d) shows estimates of the *e*-folding time ($1 / M$, in $T_c$) along with 95% confidence intervals. It is noted that the channel overlap decay *e*-folding times scale non-monotonically with $Q_v$.

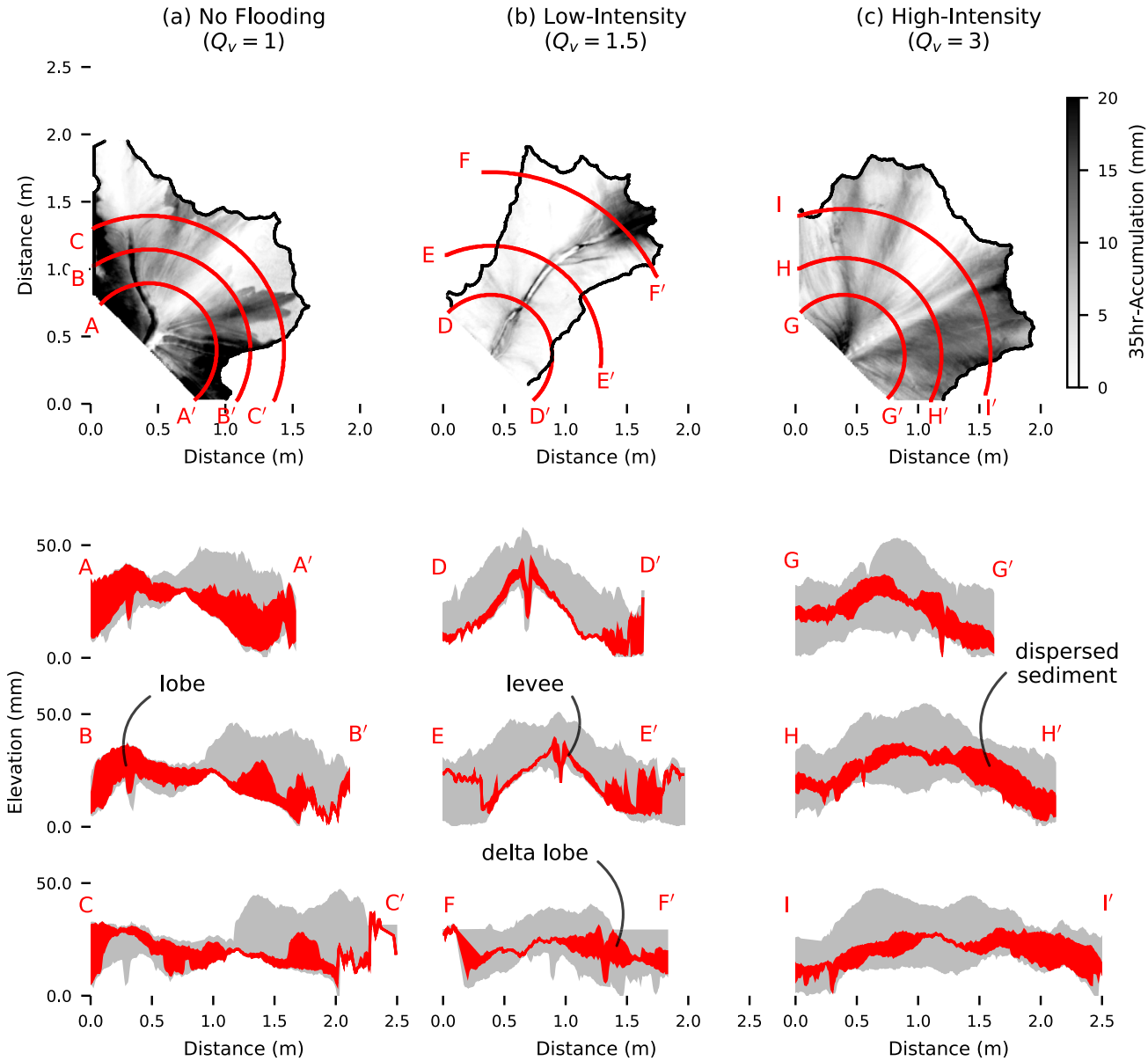


**Figure 7.** Sediment isopach maps for a sample 35 h interval across three values of $Q_v$. Dark colors indicate thicker deposition, and the shoreline is outlined for clarity. Circular sections shown in red are displayed below, where the same 35 h interval is highlighted in red, whereas the deposit for the full 100 h of runtime is shown in gray. Note that sediment thickness is variable over the illustrated interval when $Q_v = 1$ because the active delta lobe switches from one side of the delta to the other during the episode. Sediment thickness is more variable when $Q_v = 1.5$, because levees that can be seen aggrading on either flank of the channel confine flow and prevent it from being distributed laterally. In contrast, the sediment packages deposited when $Q_v = 3$, are less variable in thickness.

When flooding intensity is high ($Q_v = 3$), sediment is deposited evenly across the floodplain of the delta, indicated by consistent thickness in the isopach map. Consistent thickness of coeval deposits in proximal as well as distal stratigraphic sections also demonstrates relatively uniform deposition. When no flooding is present ($Q_v = 1$), sediment deposition is focused in delta lobes, but not to the same degree as during low-intensity flooding. In fact, lateral sediment dispersal can clearly be seen in stratigraphic sections as well as the isopach maps in Figure 7a.

Channel abundance estimates (Figure 8) show that the abundance of channels in the stratigraphic record scales non-monotonically with flooding intensity. When low-intensity flooding was imposed, channel deposits comprise a minor portion of the delta stratigraphy. In contrast, the concentration of channels in the stratigraphy increases with high-intensity flooding. When no flooding is imposed, the concentration

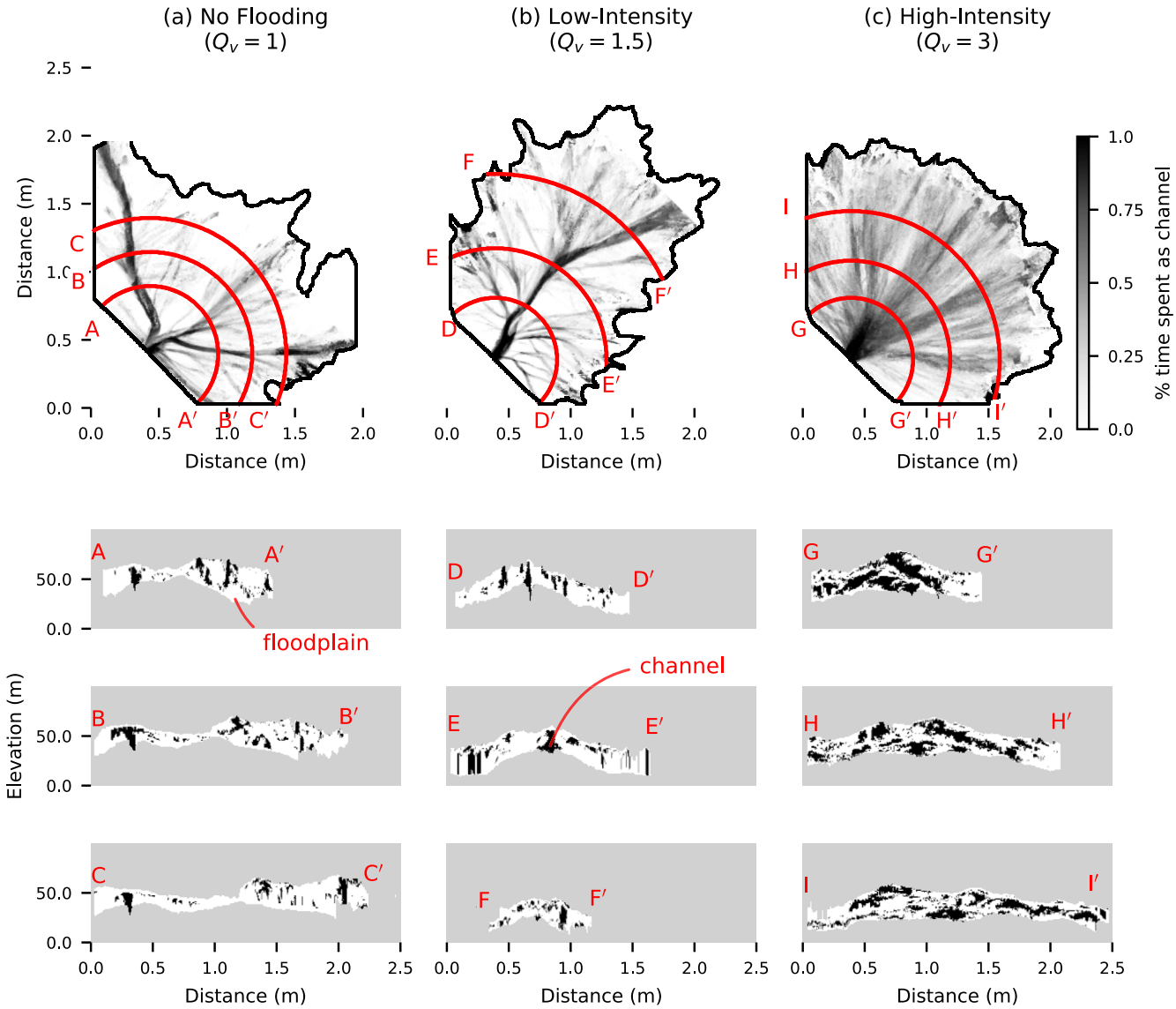


**Figure 8.** Channel abundance maps and stratigraphic sections. In stratigraphic sections, channel deposits are indicated in black, while floodplain deposition is indicated in white. In the plan-view maps, higher channel visitation is indicated by darker colors, whereas light colors demonstrate that channels rarely visited that location. Visually, it is clear that channels are more abundant in the stratigraphy when $Q_v = 3$, whereas the sections for $Q_v = 1.0$ and $Q_v = 1.5$ are less clear. The abundance of channels in the strata as a function of the radius is quantified in Figure 9.

of channels in the delta stratigraphy is intermediate, comprising a smaller proportion of the deposit than a high-intensity flooding delta, but more than a low-intensity flooding delta.

Grain size samples taken from channelized and floodplain sediments for each experimental stage show that channelized deposits are, on average, coarser than floodplain sediments (Figures 9a and 9b). Channel deposits are also relatively coarse compared to the input mixture (shown in black), whereas the floodplain deposits are relatively fine. Additionally, channel abundance consistently decreases as a function of radial distance from the delta apex (Figures 9d–9f), indicating that proximal deposits consist of a larger fraction of coarse sediment than distal deposits, on average.

Moreover, sections taken through the physical deposit also show grain size sorting during different flood regimes. Shown in Figure 10 are sections taken through the deposit at proximal and distal locations for the stages where $Q_v = 1.5$ and $Q_v = 3$. Since red sediment is a tracer of coarse material, red coloration in the deposit indicates sand deposition in these photopanels. In proximal sections (A and B), coarse material is

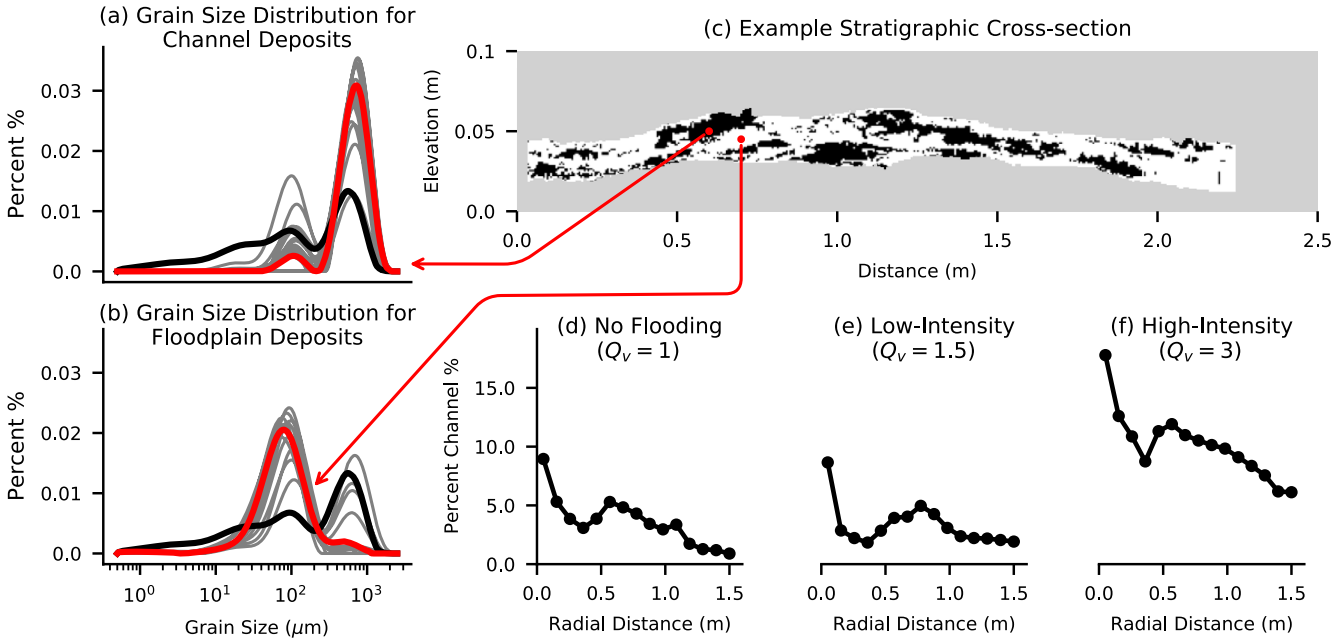


**Figure 9.** Shown in (a and b) are grain size distributions from channel and floodplain deposits identified in physical stratigraphic cuts (gray), with an example sample highlighted (red) for each facies. Also shown in black is the grain size distribution of the input sediment mixture. Shown in (d–f) are the abundance of channel deposits in circular sections taken through the synthetic stratigraphy at several radii from the delta apex. All experiments show a general basinward fining, but channel facies are more abundant when $Q_v = 3$, least abundant when $Q_v = 1.5$ and intermediate when $Q_v = 1$.

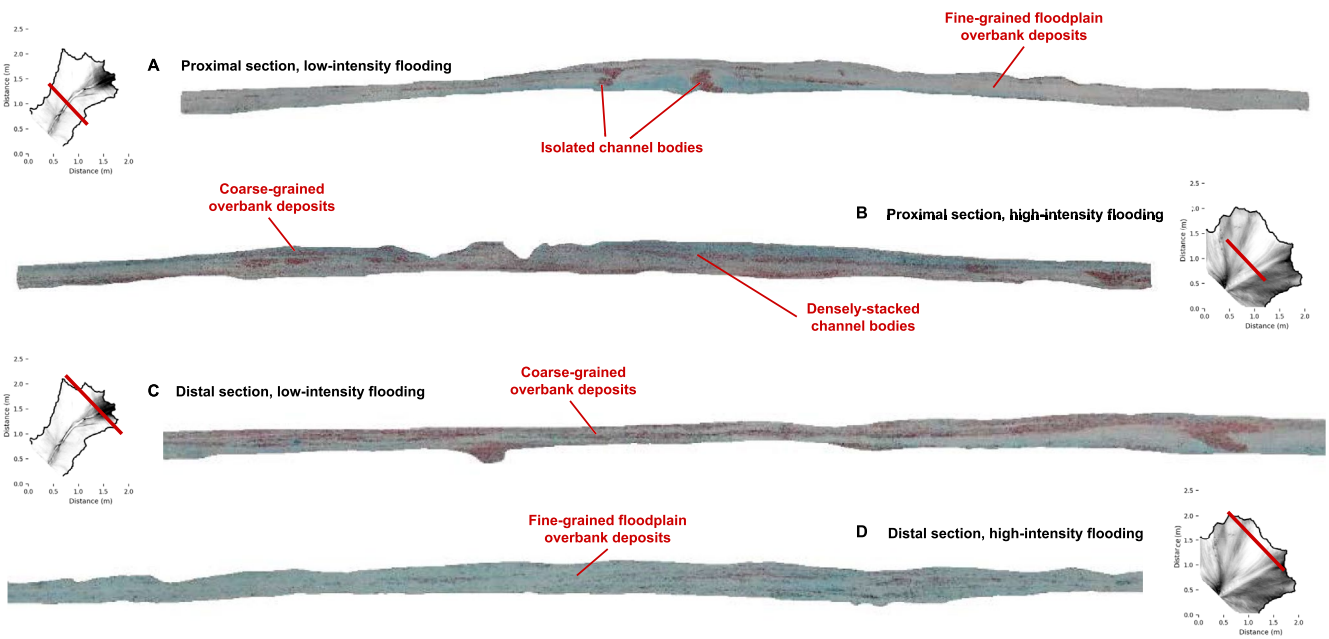


**Figure 10.** Proximal and distal sections through the experimental delta deposit. Red sand is a tracer for coarse-grained deposition. Maps show location of stratigraphic cuts in delta basin. Proximal cuts highlighting the low-intensity flooding interval (a) and high-intensity interval (b) are contrasted with distal cuts from low- (c) and high-intensity (d) flooding intervals. Note the relative concentrations and locations of red coarse-grained material, and white fine-grained material.

confined to channels during low-intensity flooding, and distributed to the overbank environment during high-intensity flooding. By contrast, in distal sections (C and D), coarse material is preferentially distributed at the shoreline during low-intensity flooding, whereas fine sediment dominates deposition during high-intensity flooding.

Finally, the evenness of sediment deposition was quantified by analyzing the growth of stratigraphic completeness as a function of discretization timescale. Extracting preservation data along a circular section of each experimental data set at a medial distance from the delta apex, the completeness of each location along the section was calculated for a range of $\delta t$ values from the finest discretization possible up to the compensation timescale. These data were modeled with Equation 10 using MCMC methods to produce posterior distributions of $\beta$. During low-intensity flooding, $\beta$ assumes a maximum value (Figures 11d), indicating uneven sediment dispersal, and a propensity to favor downstream sediment transport versus lateral sediment dispersal. In contrast, $\beta$ assumes a minimum value when $Q_v = 3$, indicating that high-intensity flooding promotes lateral sediment dispersal to evenly cover the delta topset. When $Q_v = 1$, $\beta$ assumes an intermediate value, indicating a balance between lateral versus downstream sediment dispersal.

### 3.3. Channel and Delta Floodplain Morphology

Channel geometry scaled non-monotonically in response to increasing flooding intensity (Figure 12). When no flooding was present, channel slope was $2.67 \times 10^{-2}$ on average. When low-intensity flooding was imposed, channel slopes shallowed substantially to $1.83 \times 10^{-2}$, but as flooding intensified such that $Q_v = 3$, channel slopes increased substantially to $2.69 \times 10^{-2}$. When no flooding was present, channels were 10.5 mm deep on average. When low-intensity flooding was imposed, channels deepened to 12.5 mm, but as flooding intensified such that $Q_v = 3$, channels shallowed to 8.98 mm deep. When no flooding was present, channels were 6.83 cm wide on average. When low-intensity flooding was imposed, channels narrowed to 5.76 cm wide, but as flooding intensified such that $Q_v = 3$, channels widened to 16.5 cm across (see Table 2).

When no flooding was present, floodplain relief averaged 4.91 mm. During low-intensity flooding, enhanced alluvial ridges were observed, with characteristic floodplain relief of 7.53 mm. In contrast, floodplain relief was diminished during high-intensity flooding, totaling 4.74 mm. Delta lobes at the shore grew with delivery of sediment from the river channels, creating a rugose shoreline. When no flooding was present, shoreline rugosity calculated using Equation 11, was 0.18. When low-intensity flooding was imposed, shoreline rugosity increased to 0.356, whereas when flooding intensity increased to $Q_v = 3$, shoreline rugosity decreased to 0.137.

### 3.4. Levee Breach Abundance

Counts of levee breaches conducted in each hour of the experiment indicate that levee breaches are less abundant when flood intensity is low ($Q_v = 1.5$) as compared to no flooding or high-intensity flooding. As shown in Figure 14, an average of 9.03 levee breaches were active at any given hour when there was no flooding, and when flooding was intense ($Q_v = 3$), 10.6 levee breaches were active. In contrast, when flood intensity was low, only 5.11 levee breaches were active at any given time. These results were analyzed using an ANOVA with Poisson-distributed dispersion, yielding posterior estimates summarized in Table 2.

## 4. Floods and Basin-Scale Morphodynamics

### 4.1. Channel-Floodplain Sediment Exchange

In this experimental apparatus, the main mechanism driving lateral channel mobility is avulsion. Visual observations from overhead imagery show that avulsions occurred in the experiments when channel banklines failed and subsequent erosion scoured a permanent crevasse splay, allowing water and sediment to flow onto the floodplain through the breach (Figure 14). Overbank flow is the result of sediment that accumulates in the channel and elevates the water stage above the levee crest. Thus, the key control on avulsion is the balance between in-channel aggradation, which destabilizes the channel by increasing the probability of crevasses, and the propensity to build levees, which confine the flow and preclude avulsions.

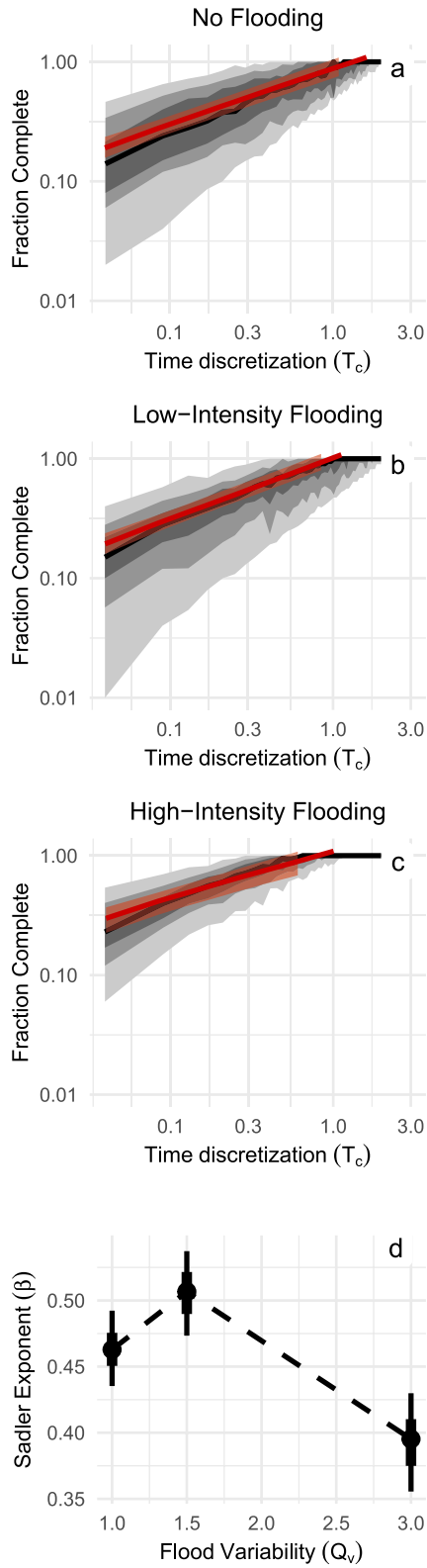
No Flooding
a
Fraction Complete
1.00
0.10
0.01
0.1
0.3
1.0
3.0
Time discretization ($T_c$)
Low−Intensity Flooding
b
Fraction Complete
1.00
0.10
0.01
0.1
0.3
1.0
3.0
Time discretization ($T_c$)
High−Intensity Flooding
c
Fraction Complete
1.00
0.10
0.01
0.1
0.3
1.0
3.0
Time discretization ($T_c$)
d
Sadler Exponent (β)
0.50
0.45
0.40
0.35
1.0
1.5
2.0
2.5
3.0
Flood Variability ($Q_v$)

**Figure 11.**

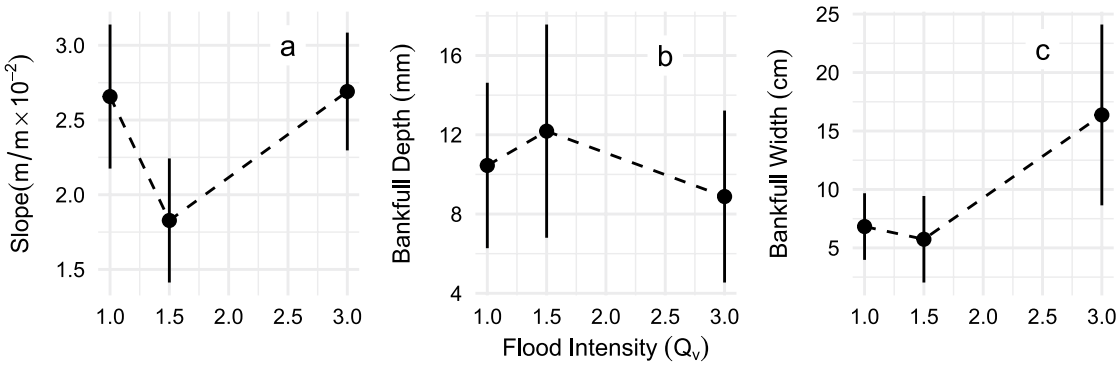


**Figure 12.** Channel geometry estimates across a gradient of $Q_v$. Points represent average values, and bars represent the mean ± the standard deviation. Channel widths, depths, and slope all scale non-monotonically with $Q_v$.

Flooding intensity impacted both of these processes. The impacts are shown in Figure 15, where the process of channel evolution is illustrated for two contrasting scenarios: $Q_v = 1.5$ and $Q_v = 3$. When flooding intensity is low, in-channel aggradation is balanced by levee aggradation (Figure 15; $A$—$A'$), which confines the flow and precludes avulsions, such that over the $1 / 2T_c$ depicted in the figure, the channel under low-intensity flooding was stationary. In contrast, rapid in-channel aggradation under high-intensity flooding outpaces levee aggradation (Figure 15; $B$—$B'$). This destabilized the channel and promoted a subsequent avulsion, which relocated flow to river right (Figure 15; $B$—$B'$). This example serves to show a general result, which is that levee breaches were less abundant under low-intensity flooding, because sediment accreted to form levees and anneal breaches. When flooding was intense or absent, breaches became more common (Figure 14). It is this balance that impacts channel mobility, delta sediment dispersal patterns, as well as channel geometries as a result of changing flood intensity.

Channel overlap $e$-folding times (Figure 6) show clearly that extreme flooding ($Q_v = 3$) promotes enhanced channel mobility, in keeping with existing evidence that flooding increases bank erosion, promoting avulsion and inhibiting levee growth (Esposito et al., 2018). Levee breaches are the nuclei for incipient avulsions, and elevated flood stages and flow velocities during peak flood conditions promoted bank erosion and scour that facilitated the avulsion process. This effect was paired with in-channel aggradation during interflood periods that primed overbank flows in the subsequent flood cycles (Figure 15). Combined, these processes promoted frequent avulsions, and intensified channel mobility, dispersing coarse material across the proximal delta.

### 4.2. An Optimum Levee-Building Condition

In contrast, our results indicate that moderate levels of flooding ($Q_v = 1.5$) inhibited channel mobility. Whereas high-intensity floods appear to limit the development of long-lived levees, low-intensity flooding clearly promotes long-term levee construction (Figure 7). Moderate floods ensured that fine sediment was delivered to channel margins during overbank conditions, and waning overbank flow velocity on the falling limb resulted in sediment deposition adjacent to the channel margin (Figure 15). Sediment supplied to channel margins thus contributed to channel confinement, by annealing levee breaches and forestalling incipient avulsions (Figure 14). However, when flow is steady ($Q_v = 1$), levee breaches are subjected to continuous overbank flow with no rising or falling limb, thus reducing the probability that levee breaches will silt and anneal. In this way, moderate flooding stabilizes levees, and in so doing, limits channel mobility

**Figure 11.** The power-law growth of stratigraphic completeness as a function of discretization timescale is shown for flooding intensity values of $Q_v = 1.0$, $Q_v = 1.5$, and $Q_v = 3.0$. The shaded regions show the distribution of the data binned for every value of $\delta t$, with the lightest band showing the 1st to 99th percentiles, the middle band showing the 10–90th percentiles, and the darkest showing the 25–75th percentiles. The binned median is shown as a black line. Model fits of Equation 10 are shown in red, with an 80% credible interval for the model predictions. Estimated posterior distributions for $\beta$ are shown in panel d, where the median is shown as a point, and the 25–75th percentiles are shown as a thick line, and the 10–90th percentiles shown as a thin line.

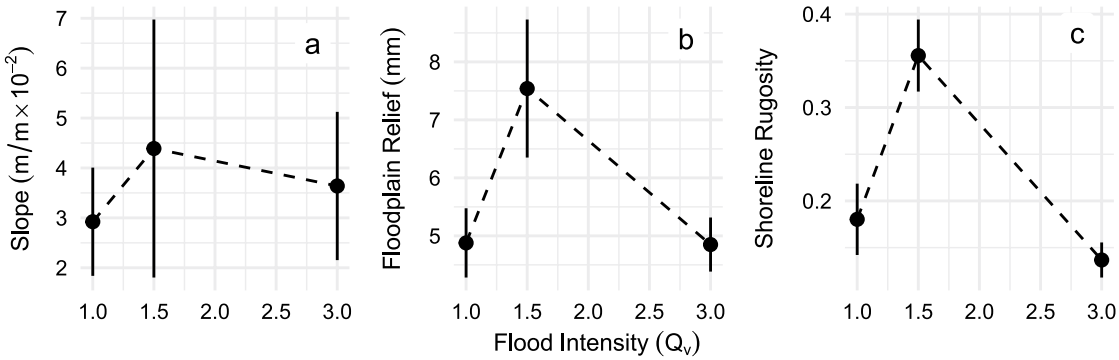


**Figure 13.** Delta morphology characteristics across a gradient of $Q_v$. Points represent average values, and bars represent the mean ± the standard deviation. Floodplain roughness, shoreline rugosity, and floodplain slope all scale non-monotonically with $Q_v$.

relative to both the high-intensity flooding and the no flooding condition, producing a non-monotonic scaling relationship (Figure 6).

These observations suggest that there exists an optimum levee-building condition between extreme levels of flood intensity (1 and 3), but since this experiment only explored three levels of flooding intensity, it is not clear whether it lies above or below $Q_v = 1.5$. In particular, levee-building requires at least some flooding to promote sediment export to the channel margins, but excess flooding increases the probability that levee breaches escalate. Moreover, the existence of an optimum levee-building condition at an intermediate level of flood intensity implies a functional relationship between $Q_v$ and levee aggradation, but the data collected in this experiment do not allow such a relationship to be derived and validated. Since these experiments do not have information about levee-building between the three levels of $Q_v$ explored here, it remains as future work to examine a gradient of $Q_v$ more finely and elucidate the location of the optimum condition. Nonetheless, the existence of an optimum due to a balance between sediment supply and levee breaching forms a framework for interpreting the non-monotonic trends observed in sediment dispersal patterns and and topography.

### 4.3. Sediment Dispersal and Topography

Levee breaching also impacts the extent of inundation and sediment dispersal across the delta topset, thereby affecting accumulation patterns. The evidence indicates that across a gradient of flooding intensities, sediment dispersal patterns exhibit non-monotonic behavior, just as with channel mobility. When no flooding is present ($Q_v = 1$), fluvial morphologies and kinematics equilibrate to time-averaged sediment flux and aggradation conditions. An incremental increase in flood amplitude to $Q_v = 1.5$ stabilized channels and confined flow, which restricted floodplain sediment deposition to the area immediately adjacent to the channel. Thus, moderate flooding focused sediment transport downstream to the channel mouth, which prograded delta lobes and led to uneven sediment package thickness and a rugose shoreline (Figure 7). A further increase in flood amplitude to $Q_v = 3$, however, produced the opposite response. By driving frequent avulsions through levee breaches, high-intensity flooding resulted in extensive lateral sediment dispersal. Sediment packages in the high-intensity flooding experiment were evenly distributed across the delta topset, in contrast to both the no-flooding condition as well as the low-intensity flood condition (Figures 7 and 11).

The non-monotonic style of fluvial sediment dispersal impacted floodplain topography and channel geometry. During high-intensity flooding, frequent avulsions evenly spread sediment across the delta topset, which resulted in muted floodplain roughness (Figure 13). Furthermore, because channels were short-lived due to the frequency of avulsions, basinward progradation of delta lobes was inhibited, and shoreline rugosity was diminished (Figure 13). In contrast, during low-intensity flooding, stable channels limited lateral sediment dispersal, and focused deposition adjacent to the channel, thus accentuating floodplain roughness (Figures 7 and 11). With restricted mobility, channels under low-intensity flooding acted as conduits

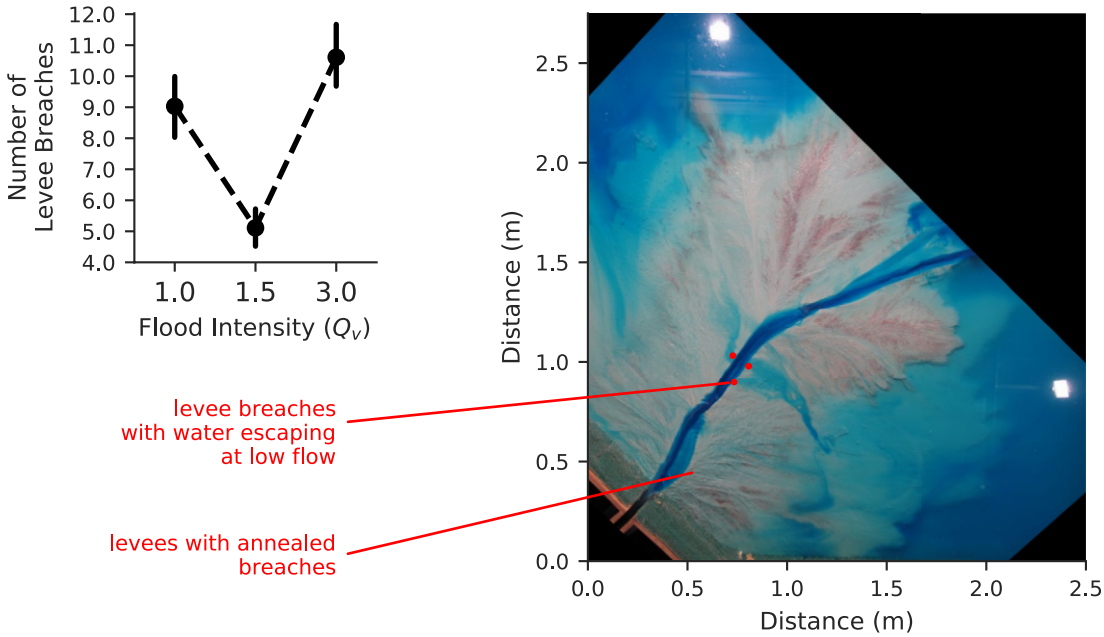


**Figure 14.** Counts of active levee breaches during each hour of the experiment across a gradient in flooding intensity. Levee breaches were most common during high-intensity flooding. Levee breaches were less abundant during low-intensity flooding as compared to either no flooding or high-intensity flooding. Shown is an example overhead image at low flow, where levee breaches were identified as locations where flow escaped from the channel to the floodplain. The location of levee breaches that annealed is also indicated.

to transport sediment to the shoreline, promoting lobe progradation and enhanced shoreline rugosity (Figure 13).

Levee-building processes are also reflected in channel geometries, which display non-monotonic scaling with flood intensity (Figure 12). Enhanced erosion of levees and frequent avulsion during high-intensity flooding leads to the formation of broad, shallow channels. Sustained levee aggradation during low-intensity flooding produces relatively deep, narrow channels. Intermediate levee-building under constant flow thus resulted in channels of intermediate dimensions (Figure 12). Variation in channel slope reflects the fact that when levees prevent avulsion or lateral migration, delta lobes prograde into the basin, while the channel apex remains in place; this lengthens the channel relative to the vertical drop, decreasing the slope. Intriguingly, while the channel geometry models developed by Blom et al. (2017) and Naito and Parker (2019) disagree about the manner in which channel geometry should scale with increasing $Q_v$, they both predict that channel width, depth, and slope should scale *monotonically* with increasing $Q_v$, contrary to our results. It is important that neither of these models explicitly incorporates the lateral distribution of sediment across the channel margin as a process influencing channel geometry at steady-state. The contradiction between these models of channel evolution and our observations suggests that the existence of a levee-building optimum is an important but overlooked aspect of fluvial morphodynamics that fundamentally changes predictions of landscape evolution under variable flow.

## 5. Generalization and Applications

### 5.1. Optimum Levee-Building at the Field Scale

Extending these results from the laboratory to field scale systems requires care. In these experiments, levee aggradation is the key process generating non-monotonicity, but in natural rivers, many processes influence the exchange of sediment and water between channels and the adjacent floodplains (Mertes et al., 1995; Adams et al., 2004; Lewin et al., 2017). Instead of considering the direct processes of levee construction, which is still poorly understood at the field scale (Johnston et al., 2019), we propose a framework that considers a balance between processes that *nourish* the channel margin with sediment versus processes that *deplete* the channel margin of sediment. Many natural river systems, like the Saskatchewan River (Saskatchewan,

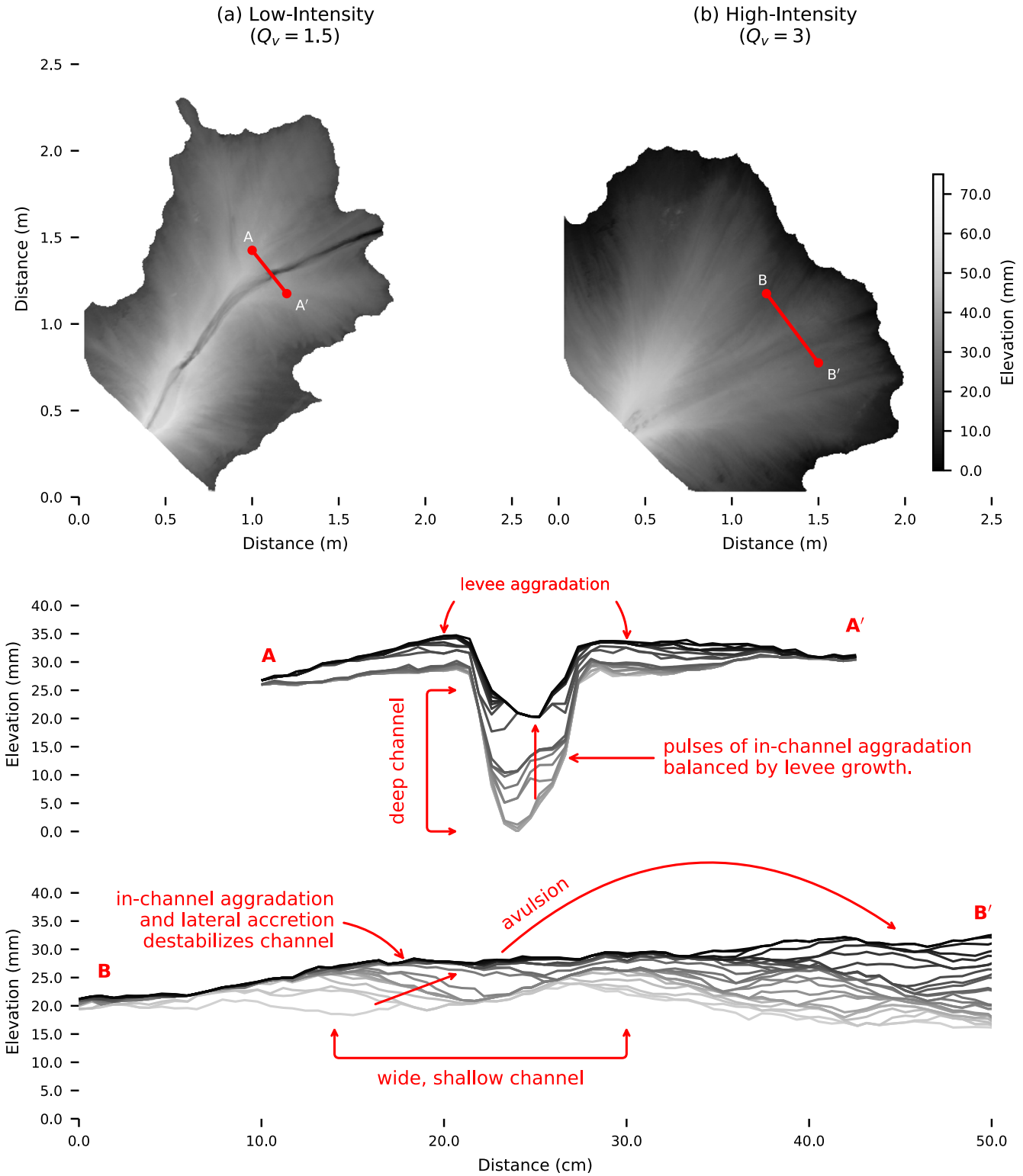


**Figure 15.** Topographic maps of two example stratigraphic surfaces are shown in (a and b), with transects marked $A$—$A'$ and $B$—$B'$. Transects are shown in the corresponding lower panels. Shown in gray lines are successive stratigraphic surfaces, demonstrating sediment deposition patterns. Darker surfaces are younger, and lighter surfaces are older. Note that in transect $A$—$A'$, initial channel scouring is followed by subsequent in-channel aggradation, which would lead to avulsion except for the fact that levee aggradation confines the channel, and restricts it to one location. In contrast, transect $B$—$B'$ shows initial levee aggradation, but levee development does not continue, and in-channel aggradation forces an avulsion to river right.

Canada) receive channel bank deposition by advection, where lateral head gradients drive flow transverse to the channel, building wide, low levees (Adams et al., 2004). In this case, it is likely that an incremental increase in flood intensity will enhance lateral advection of sediment, eroding levee crests and depleting the channel margins of sediment, similar to our results comparing $Q_v = 1.5$ and $Q_v = 3$.

In contrast, on reaches of the Columbia River (BC, Canada), also studied by Adams et al. (2004), levee construction is dominated by diffusive transport. Sediment is confined near the river channel, constructing relatively narrow levees. In this scenario, an incremental increase in flood intensity could promote more advective transport to the channel margins, nourishing the banks with additional sediment. While the effect of $Q_v$ on patterns of channel bank nourishment has not been studied in the field, we suspect that natural systems fall along a similar gradient as our experiments. To identify this effect in the field though, it will be necessary to control for differences in vegetation, sediment texture, geologic history, land use, and local hydrology, among others.

Moreover, because of differences in processes, the values of $Q_v$ presented in this experimental study will likely not translate directly to field-scale systems. Instead, for a given river reach, it would be reasonable to calculate $Q_v$ using hydrograph data, then normalize this value with an appropriate scaling factor to compare it to our experiments. For example, $Q_v = 3$ is the maximum sustainable value in our experiments because above that value, the river fails to channelize. Thus, the maximum sustainable value for a field site could be estimated by looking at comparable river systems with more intense floods, and then used to scale the value for the field site in question. There are clear issues with this approach—there is no reason to think that the response curve scales proportionally—but it would be a reasonable first step to bridge these experimental findings to field data.

### 5.2. Flooding in the Stratigraphic Record

When attempting to infer alluvial dynamics from the geologic record, the distinction between channel deposits and overbank deposits, their relative abundance, and their spatial relationships form the crux of the process interpretation. These deposits are most clearly recognized by changes in grain size. For example, variation in the abundance of coarse versus fine grains have been interpreted to reflect changes in boundary conditions like enhanced mountain uplift or changes in base level (e.g., Heller & Paola, 1992). Our results show conclusively that grain-size variation can occur simply because of a change in flood intensity (Figure 10), whereby grain sizes are sorted and partitioned both laterally and longitudinally by different intensities of overbank flow. However, the expression of a given stratigraphic exposure may have several plausible root causes, and so detailed observations of sedimentary structures are needed to distinguish between them.

Various metrics and facies associations have been proposed as diagnostic of alluvial systems experiencing extreme floods (e.g., Plink-Björklund, 2015), but in general, the specific mechanisms by which changes in flood intensity are expressed in the strata have remained underconstrained. This study: (a) identifies levee-building as a definitive mechanism governing the spatial allocation of grain sizes and sediment in fluvio-deltaic systems undergoing variable flow, and (b) demonstrates that this mechanism is responsible for non-monotonic dynamics across a gradient in flooding intensity. Thus, stratigraphic interpretations of flooding intensity from field outcrops should target levee deposits as the main focus for inferring the level of flooding intensity.

Moreover, the non-monotonic behavior suggests that changes in flooding may manifest differently depending on whether the current level of flooding is above or below the optimum for levee construction. For example, prior to the Paleocene-Eocene Thermal Maximum (PETM, ~55.6 Ma, Kennett & Stott (1991)), rivers in the Piceance Basin (Colorado, USA) were likely characterized by low-intensity flooding. However, during the PETM, enhanced flooding destabilized Piceance rivers, by driving overbank flow and crevassing (Foreman et al., 2012). This likely indicates that enhanced flooding during the PETM pushed flood intensity beyond the optimum condition for levee construction in the Piceance floodplain. However, another basin may have a different response. For example, if intensified flooding in another basin brought the system state closer to its optimum levee condition, channels may have stabilized.

These changes in alluvial dynamics relative to the levee-building optimum are likely to influence the preservation potential of sedimentary deposits. Almost all sedimentary systems comprise a hierarchy of

morphodynamic scales. That is, there are multiple classes of self-organized sedimentary structures that share a characteristic size and migration velocity. Recent work has shown that changes in the relative migration rates of these hierarchical elements is a useful framework for interpreting the completeness of sedimentary deposits (Ganti et al., 2020). Our experiments comprise two morphdynamic hierarchies: (a) channels, and (b) delta lobes. The estimates of channel mobility in Figure 6 do not discriminate between channel and lobe migration, but visual observations indicate that the channel migration rate is much the same across flooding intensity levels. That is, we observed that in all cases, the cohesive banks of channels are not easily eroded, and channels rarely cut laterally to migrate. However, the lobe avulsion rate decelerated substantially near the levee-building optimum, and accelerated away from the optimum. In other words, near the optimum condition, the migration rate of the largest hierarchy approaches the migration rate of the smallest hierarchy. Thus, according to the framework in Ganti et al. (2020), deposits generated by low-intensity flooding should preferentially preserve medial elevations due to low stratigraphic completeness and a lack of reworking, which is what we find in Figure 11.

### 5.3. Future Climate Impacts

The existence of a levee-building optimum also impacts projections of the fluvial response to future climate change. Changes in precipitation due to global warming are expected to result in enhanced flooding in some regions and diminished flooding in others. This study suggests that the fluvial response will depend on the system state relative to the levee-building optimum. In regions where the flood intensity is below the optimum level for levee construction, enhanced flooding may cause future channel stabilization. On the other hand, a counterintuitive implication is that if flood intensity in a region is at or below its optimum for levee-building, a decrease in flood intensity may, in fact, destabilize channels.

## 6. Conclusions

Variable flow is a natural condition for all river channels, yet its impacts on fluvio-deltaic morphodynamics are difficult to predict. This study evaluated the impact of flooding intensity on fluvial dynamics using a set of three physical delta experiments that spanned a gradient of flood intensity ($Q_v$). In each experiment, the time-averaged sediment and water flux were held constant while channel mobility, sediment dispersal, and landscape morphology were observed.

When no flooding was present ($Q_v = 1$), channels were flanked by discontinuous levees, which restricted channel mobility and produced a characteristic width and depth. Levee breaches, crevassing and avulsion events were the primary mechanisms to deliver sediment to the floodplain, building delta lobes and producing a rugose shoreline.

When low-amplitude floods ($Q_v = 1.5$) were imposed, sediment was consistently delivered to levee crests with every flood cycle. As a result, levee breaches tended to anneal over successive flood waves, and channels deepened and narrowed, while cohesive channel banks severely decreased channel mobility. Tall levees confined flow and restricted the locus of deposition to areas immediately adjacent to the channel margin and lobes at the delta shoreline. The outcome of this was to enhance shoreline rugosity, lower channel slopes, and construct substantial floodplain relief.

However, when flood amplitude increased to $Q_v = 3$, vigorous overbank flow advected sediment beyond channel margins, exacerbating existing levee breaches, and shortening the avulsion frequency. This process inhibited levee aggradation and promoted enhanced bank erosion, which created wide, shallow channels characterized by rapid planform mobility. Low channel margins primed the system for substantial overbank flow, and promoted lateral sediment dispersal across the delta topset. Floodplain relief decreased as a result of even sediment deposition, and enhanced channel mobility precluded the development of long delta lobes. Combined, these processes produced higher channel slopes and lower shoreline rugosity.

Taken together, these observations of fluvio-deltaic morphologies and kinematics show that surface processes and sediment dispersal scale non-monotonically across three levels of flooding intensity. Flooding induces a morphodynamic feedback in the fluvial system, where flood amplitude determines the inundation extent, thereby altering erosion and deposition patterns and shaping fluvio-deltaic morphology, which

in turn impacts overbank flow. Levees are the lynchpin of this feedback, governing sediment exchange between channels and adjacent floodplains. Below the intermediate value of flood amplitude, marginal increases in flood intensity stabilized levees, whereas a marginal increase in flooding intensity destabilized levees, suggesting the existence of an optimum value. While these observations do not precisely constrain the location of the optimum levee building condition, our results demonstrate that extreme values of flood intensity induce a cascade of impacts on fluvial dynamics across scales. Importantly, since each experiment was run with the same equivalent steady discharge, these results suggest that in fan deltas with variable flow, levee construction processes may be an essential component needed to accurately model landscape evolution and interpret fluvio-deltaic stratigraphy.

## Data Availability Statement

Data products and software necessary for recreating this study are available in a Zenodo repository (https://doi.org/10.5281/zenodo.4928815), and Github repository (https://doi.org/10.5281/zenodo.4929108), respectively. Some analyses are derived from the TDB 12-1 data set, available on SEAD (https://doi.org/10.5967/M03N21GX).

**Acknowledgments**
Eric Barefoot would like to thank Robert Mahon for his hospitality while conducting these experiments, and to Ripul Dutt for assistance and training. Eric Barefoot acknowledges support from a Pathfinder Fellowship provided by CUAHSI with support from the National Science Foundation (NSF) Cooperative Agreement No. EAR-1849458. Eric Barefoot additionally acknowledges support from SEPM via a Student Assistance Grant. The authors also acknowledge helpful reviews from Kenuske Naito and two anonymous reviewers, whose feedback substantially improved the manuscript.

## References

Adams, P. N., Slingerland, R. L., & Smith, N. D. (2004). Variations in natural levee morphology in anastomosed channel flood plain complexes. *Geomorphology*, *61*(1), 127–142. Retrieved from https://doi.org/10.1016/j.geomorph.2003.10.005

Blom, A., Arkesteijn, L., Chavarrías, V., & Viparelli, E. (2017). The equilibrium alluvial river under variable flow and its channel-forming discharge. *Journal of Geophysical Research: Earth Surface*, *122*(10), 1924–1948. Retrieved from https://doi.org/10.1002/2017jf004213

Bryant, M., Falk, P., & Paola, C. (1995). Experimental study of avulsion frequency and rate of deposition. *Geology*, *23*(4), 365–368. https://doi.org/10.1130/0091-7613(1995)023<0365:esoafa>2.3.co;2

Chamberlin, E. P., & Hajek, E. A. (2015). Interpreting paleo-avulsion dynamics from multistory sand bodies. *Journal of Sedimentary Research*, *85*(2), 82–94. https://doi.org/10.2110/jsr.2015.09

Engelund, F., & Hansen, E. (1967). A monograph on sediment transport in alluvial streams (Vol. 10). Technical University of Denmark 0stervoldgade. Retrieved from https://repository.tudelft.nl/islandora/object/uuid:81101b08-04b5-4082-9121-861949c336c9

Eschner, T. R., Hadley, R. F., & Crowley, K. D. (1981). *Hydrologic and morphologic changes in channels of the platte river basin: A historical perspective*. U.S. Geological Survey.

Esposito, C. R., Leonardo, D. D., Harlan, M., & Straub, K. M. (2018). Sediment storage partitioning in alluvial stratigraphy: The influence of discharge variability. *Journal of Sedimentary Research*, *88*(6), 717–726. Retrieved from https://doi.org/10.2110/jsr.2018.36

Fielding, C. R., Alexander, J., & Allen, J. P. (2018). The role of discharge variability in the formation and preservation of alluvial sediment bodies. *Sedimentary Geology*, *365*, 1–20. Retrieved from https://doi.org/10.1016/j.sedgeo.2017.12.022

Foreman, B. Z., Heller, P. L., & Clementz, M. T. (2012). Fluvial response to abrupt global warming at the Palaeocene/Eocene boundary. *Nature*, *491*(7422), 92–95. Retrieved from https://doi.org/10.1038/nature11513

Ganti, V., Hajek, E. A., Leary, K., Straub, K. M., & Paola, C. (2020). Morphodynamic Hierarchy and the Fabric of the Sedimentary Record. *Geophysical Research Letters*, *47*(14). Retrieved from https://doi.org/10.1029/2020gl087921

Heller, P. L., & Paola, C. (1992). The large-scale dynamics of grain-size variation in alluvial basins, 2: Application to syntectonic conglomerate. *Basin Research*, *4*(2), 91–102. Retrieved from https://doi.org/10.1111/j.1365-2117.1992.tb00146.x

Hoyal, D. C. J. D., & Sheets, B. A. (2009). Morphodynamic evolution of experimental cohesive deltas. *Journal of Geophysical Research*, *114*(F2). https://doi.org/10.1029/2007jf000882

Jerolmack, D. J., & Sadler, P. (2018). Transience and persistence in the depositional record of continental margins. *Journal of Geophysical Research: Earth Surface*, *112*, F03S13. J. Retrieved from https://doi.org/10.1029/2006JF000555

Johnston, G. H., David, S. R., & Edmonds, D. A. (2019). Connecting Fluvial Levee Deposition to Flood-Basin Hydrology. *Journal of Geophysical Research: Earth Surface*, *124*(7), 1996–2012. https://doi.org/10.1029/2019jf005014

Kennett, J. P., & Stott, L. D. (1991). Abrupt deep-sea warming, paleoceanographic changes and benthic extinctions at the end of the Palaeocene. *Nature*, *353*(6341), 225–229. Retrieved from https://doi.org/10.1038/353225a0

Kim, W., Paola, C., Swenson, J. B., & Voller, V. R. (2006). Shoreline response to autogenic processes of sediment storage and release in the fluvial system. *Journal of Geophysical Research*, *111*(F4). Retrieved from https://doi.org/10.1029/2006jf000470

Latrubesse, E. M., Stevaux, J. C., & Sinha, R. (2005). September). Tropical rivers. *Geomorphology*, *70*(3), 187–206. Retrieved from https://doi.org/10.1016/j.geomorph.2005.02.005

Lauer, J. W., & Parker, G. (2008). Modeling framework for sediment deposition, storage, and evacuation in the oodplain of a meandering river: Application to the Clark Fork River, Montana. *Water Resources Research*, *44*(8). https://doi.org/10.1029/2006WR005529

Leeder, M. R. (1977). A quantitative stratigraphic model for alluvium, with special reference to channel deposit density and interconnectedness. *Fluvial Sedimentology*, *5*, 587–596. Retrieved from http://archives.datapages.com/data/dgs/005/005001/587_cspgsp0050587.htm

Leier, A. L., DeCelles, P. G., & Pelletier, J. D. (2005). Mountains, monsoons, and megafans. *Geology*, *33*(4), 289–292. Retrieved from https://doi.org/10.1130/g21228.1

Leopold, L., & Maddock, T., Jr. (1953). *The hydraulic geometry of stream channels and some physiographic implications (USGS Numbered Series No. 252)*. Retrieved from http://pubs.er.usgs.gov/publication/pp252

Lewin, J., Ashworth, P. J., & Strick, R. J. P. (2017). Spillage sedimentation on large river floodplains. *Earth Surface Processes and Landforms*, *42*(2), 290–305. https://doi.org/10.1002/esp.3996

Li, Q., Yu, L., & Straub, K. M. (2016). Storage thresholds for relative sea-level signals in the stratigraphic record. *Geology*, *44*(3), 179–182. https://doi.org/10.1130/g37484.1

Mertes, L. A. K. (1994). Rates of flood-plain sedimentation on the central Amazon River. *Geology*, *22*(2), 171–174. https://doi.org/10.1130/0091-7613(1994)022<0171:rofpso>2.3.co;2

Mertes, L. A. K., Daniel, D. L., Melack, J. M., Nelson, B., Martinelli, L. A., & Forsberg, B. R. (1995). Spatial patterns of hydrology, geomorphology, and vegetation on the floodplain of the Amazon river in Brazil from a remote sensing perspective. *Geomorphology*, *13*(1), 215–232. Retrieved from https://doi.org/10.1016/b978-0-444-81867-6.50018-6

Miller, K. L., Kim, W., & McElroy, B. (2019). Laboratory Investigation on Effects of Flood Intermittency on Fan Delta Dynamics. *Journal of Geophysical Research: Earth Surface*, *124*(2), 383–399. https://doi.org/10.1029/2017jf004576

Mohrig, D., Heller, P. L., Paola, C., & Lyons, W. J. (2000). Interpreting avulsion process from ancient alluvial sequences: Guadalope-Matarranya system (northern Spain) and Wasatch Formation (western Colorado). *Geological Society of America Bulletin*, *112*(12), 1787–1803. Retrieved from https://doi.org/10.1130/0016-7606(2000)112<1787:iapfaa>2.0.co;2

Naito, K., & Parker, G. (2019). Can bankfull discharge and bankfull channel characteristics of an alluvial meandering river be cospecified from a flow duration curve? *Journal of Geophysical Research: Earth Surface*, *124*(10), 2381–2401. Retrieved from https://doi.org/10.1029/2018jf004971

Nittrouer, J. A., Allison, M. A., & Campanella, R. (2008). Bedform transport rates for the lowermost Mississippi River. *Journal of Geophysical Research*, *113*(F3), F03004. https://doi.org/10.1029/2007jf000795

Parker, G., Paola, C., Whipple, K. X., & Mohrig, D. (1998). Alluvial fans formed by channelized fluvial and sheet flow. I: Theory. *Journal of Hydraulic Engineering*, *124*(10), 985–995. Retrieved from https://doi.org/10.1061/(ASCE)0733-9429(1998)124:10(985)

Parker, G., Shimizu, Y., Wilkerson, G. V., Eke, E. C., Abad, J. D., Lauer, J. W., et al. (2011). A new framework for modeling the migration of meandering rivers. *Earth Surface Processes and Landforms*, *36*(1), 70–86. https://doi.org/10.1002/esp.2113

Pickup, G., & Rieger, W. A. (1979). A conceptual model of the relationship between channel characteristics and discharge. *Earth Surface Processes*, *4*(1), 37–42. https://doi.org/10.1002/esp.3290040104

Pizzuto, J. E. (1986). Flow variability and the bankfull depth of sand-bed streams of the American midwest. *Earth Surface Processes and Landforms*, *11*(4), 441–450. https://doi.org/10.1002/esp.3290110409

Plink-Björklund, P. (2015). Morphodynamics of rivers strongly affected by monsoon precipitation: Review of depositional style and forcing factors. *Sedimentary Geology*, *323*, 110–147. Retrieved from https://doi.org/10.1016/j.sedgeo.2015.04.004

Sadler, P. M. (1981). Sediment accumulation rates and the completeness of stratigraphic sections. *The Journal of Geology*, *89*(5), 569–584. Retrieved from https://doi.org/10.1086/628623

Straub, K. M., Duller, R. A., Foreman, B. Z., & Hajek, E. A. (2020). Buffered, Incomplete, and Shredded: The challenges of reading an imperfect stratigraphic record. *Journal of Geophysical Research: Earth Surface*, *125*(3), e2019JF005079. Retrieved from https://doi.org/10.1029/2019jf005079

Straub, K. M., Li, Q., & Benson, W. M. (2015). Influence of sediment cohesion on deltaic shoreline dynamics and bulk sediment retention: A laboratory study. *Geophysical Research Letters*, *42*(22), 9808–9815. https://doi.org/10.1002/2015gl066131

Strong, N., & Paola, C. (2008). Valleys that never were: Time surfaces versus stratigraphic surfaces. *Journal of Sedimentary Research*, *78*(8), 579–593. https://doi.org/10.2110/jsr.2008.059

Van De Lageweg, W. I., Dijk, W. M. V., & Kleinhans, M. G. (2013). Morphological and stratigraphical signature of floods in a braided gravel-bed river revealed from flume experiments. *Journal of Sedimentary Research*, *83*(11), 1033–1046. https://doi.org/10.2110/jsr.2013.70

Venables, W. N., & Ripley, B. D. (2002). *Modern applied statistics with S* (4th ed.). Springer.

Wang, Y., Straub, K. M., & Hajek, E. A. (2011). Scale-dependent compensational stacking: An estimate of autogenic time scales in channelized sedimentary deposits. *Geology*, *39*(9), 811–814. https://doi.org/10.1130/g32068.1

Wickert, A. D., Martin, J. M., Tal, M., Kim, W., Sheets, B., & Paola, C. (2013). River channel lateral mobility: Metrics, time scales, and controls. *Journal of Geophysical Research: Earth Surface*, *118*(2), 396–412. https://doi.org/10.1029/2012jf002386

Wolman, M. G., & Miller, J. P. (1960). Magnitude and frequency of forces in geomorphic processes. *The Journal of Geology*, *68*(1), 54–74. Retrieved from https://doi.org/10.1086/626637